REPORT DOCUMENTATION PAGE

Form Approved OMB NO. 0704-0188

The public reporting burden for this collection of information is estimated to average 1 hour per response, including the time for reviewing instructions, searching existing data sources, gathering and maintaining the data needed, and completing and reviewing the collection of information. Send comments regarding this burden estimate or any other aspect of this collection of information, including suggesstions for reducing this burden, to Washington Headquarters Services, Directorate for Information Operations and Reports, 1215 Jefferson Davis Highway, Suite 1204, Arlington VA, 22202-4302. Respondents should be aware that notwithstanding any other provision of law, no person shall be subject to any oenalty for failing to comply with a collection of information if it does not display a currently valid OMB control number.
PLEASE DO NOT RETURN YOUR FORM TO THE ABOVE ADDRESS.

1. REPORT DATE (DD-MM-YYYY)	2. REPORT TYPE	3. DATES COVERED (From - To)
05-01-2016	Final Report	1-Feb-2012 - 30-Sep-2015

4. TITLE AND SUBTITLE

Final Report: Near-field Nanoscopy of Metal-Insulator Phase Transitions Towards Synthesis of Novel Correlated Transition Metal Oxides and Their Interaction with Plasmon Resonances

5a. CONTRACT NUMBER
W911NF-12-1-0076

5b. GRANT NUMBER

5c. PROGRAM ELEMENT NUMBER
206022

6. AUTHORS
Shahab Derakhshan, Yohannes Abate

5d. PROJECT NUMBER

5e. TASK NUMBER

5f. WORK UNIT NUMBER

7. PERFORMING ORGANIZATION NAMES AND ADDRESSES
California State University - Long Beach
California State University Long Beach Foundation
6300 State University Drive, Ste. 332
Long Beach, CA 90815 -4670

8. PERFORMING ORGANIZATION REPORT NUMBER

9. SPONSORING/MONITORING AGENCY NAME(S) AND ADDRESS (ES)
U.S. Army Research Office
P.O. Box 12211
Research Triangle Park, NC 27709-2211

10. SPONSOR/MONITOR'S ACRONYM(S)
ARO

11. SPONSOR/MONITOR'S REPORT NUMBER(S)
60430-MS-REP.26

12. DISTRIBUTION AVAILIBILITY STATEMENT
Approved for Public Release; Distribution Unlimited

13. SUPPLEMENTARY NOTES
The views, opinions and/or findings contained in this report are those of the author(s) and should not contrued as an official Department of the Army position, policy or decision, unless so designated by other documentation.

14. ABSTRACT
The performed project was centered around two separate, albeit related topics. The high-resolution infrared near-field imaging experiments were performed to better understand the origin of emergence of metal insulator transitions (MIT) in known transition metal oxides and to utilize the phase transtion states of VO2 to control and manipulate local plasmon resonaces. First, we imaged the charge dynamics in (MIT) of both amorphous VO2 films and stress free suspended VO2 crystals and probed the existence of mixed phases in tapered suspended crystal VO2 beams. Then we studied the interaction of VO2 with plasmons. Both the film VO2 and the crystal VO2 were

15. SUBJECT TERMS
metal insulator transition, phase transition, nanoscopy, correlated materials, transition metal oxides

16. SECURITY CLASSIFICATION OF:			17. LIMITATION OF ABSTRACT	15. NUMBER OF PAGES	19a. NAME OF RESPONSIBLE PERSON
a. REPORT	b. ABSTRACT	c. THIS PAGE			Shahab Derakshan
UU	UU	UU	UU		19b. TELEPHONE NUMBER 562-985-4865

Standard Form 298 (Rev 8/98)
Prescribed by ANSI Std. Z39.18

Report Title

Final Report: Near-field Nanoscopy of Metal-Insulator Phase Transitions Towards Synthesis of Novel Correlated Transition Metal Oxides and Their Interaction with Plasmon Resonances

ABSTRACT

The performed project was centered around two separate, albeit related topics. The high-resolution infrared near-field imaging experiments were performed to better understand the origin of emergence of metal insulator transitions (MIT) in known transition metal oxides and to utilize the phase transtion states of VO2 to control and manipulate local plasmon resonaces. First, we imaged the charge dynamics in (MIT) of both amorphous VO2 films and stress free suspended VO2 crystals and probed the existence of mixed phases in tapered suspended crystal VO2 beams. Then we studied the interaction of VO2 with plasmons. Both the film VO2 and the crystal VO2 were explored for local unprecedented control of local plasmon light concentrations. We have demonstrated for the first time dynamic reversible switching of VO2 metal-insulator transition and control of plasmonic nanoantennas dipolar modes.

The other component of the work was an exploratory synthesis of novel transition metal oxides and chalcogenides, which resulted in discovery of novel phases such as BaYFeO4, CaGaYO4, Li4MgOsO6, Li4NiOsO6, Li3Ni2OsO6, La3Si1-xAlxCuQ7 (Q = S, Se) and Ca2ScOsO6. We successfully synthesized the single-phase samples of the above-mentioned phases and investigated their crystal structures and physical properties.

Enter List of papers submitted or published that acknowledge ARO support from the start of the project to the date of this printing. List the papers, including journal references, in the following categories:

(a) Papers published in peer-reviewed journals (N/A for none)

Received		Paper
01/04/2016	25.00	Phuong-Hieu T. Nguyen, Farshid Ramezanipour, John E. Greedan, Lachlan M. D. Cranswick, Shahab Derakhshan. Synthesis, Crystal Structure, and Magnetic Properties of LiLi3Mg2OsO6, a Geometrically Frustrated Osmium(V) Oxide with an Ordered Rock Salt Structure: Comparison with Isostructural Li3Mg2RuO6, Inorganic Chemistry, (11 2012): 11493. doi: 10.1021/ic3013377
08/29/2014	8.00	Jia Zhu, Kedar Hippalgaonkar, Sheng Shen, Kevin Wang, Yohannes Abate, Sangwook Lee, Junqiao Wu, Xiaobo Yin, Arun Majumdar, Xiang Zhang. Temperature-Gated Thermal Rectifier for Active Heat Flow Control, Nano Letters, (08 2014): 0. doi: 10.1021/nl502261m
08/29/2014	11.00	Corey M. Thompson, John E. Greedan, V. Ovidiu Garlea, Roxana Flacau, Malinda Tan, Phuong-Hieu T. Nguyen, Friederike Wrobel, Shahab Derakhshan. Partial Spin Ordering and Complex Magnetic Structure in BaYFeO, Inorganic Chemistry, (01 2014): 0. doi: 10.1021/ic4026798
08/29/2014	10.00	Ryan Clark, Sarah Jiaxin Zhu, Shou-Tian Zheng, Xianhui Bu, Shahab Derakhshan. CaYGaO4; a fully ordered novel olivine type gallate, Journal of Alloys and Compounds, (12 2014): 0. doi: 10.1016/j.jallcom.2014.07.121
12/30/2015	9.00	Young-Seok Shon, Dayeon Judy Shon, Van Truong, Diego J. Gavia, Raul Torrico, Yohannes Abate. Heat-induced coarsening of layer-by-layer assembled mixed Au and Pd nanoparticles, , (03 2014): 0. doi: 10.12989/anr.2014.2.1.057
12/30/2015	19.00	Yohannes Abate, Robert E. Marvel, Jed I. Ziegler, Sampath Gamage, Mohammad H. Javani, Mark I. Stockman, Richard F. Haglund. Control of plasmonic nanoantennas by reversible metal-insulator transition, Scientific Reports, (09 2015): 0. doi: 10.1038/srep13997

TOTAL: **6**

Number of Papers published in peer-reviewed journals:

(b) Papers published in non-peer-reviewed journals (N/A for none)

Received Paper

TOTAL:

Number of Papers published in non peer-reviewed journals:

(c) Presentations

Number of Presentations: 32.00

Non Peer-Reviewed Conference Proceeding publications (other than abstracts):

Received Paper

TOTAL:

Number of Non Peer-Reviewed Conference Proceeding publications (other than abstracts):

Peer-Reviewed Conference Proceeding publications (other than abstracts):

Received Paper

TOTAL:

Number of Peer-Reviewed Conference Proceeding publications (other than abstracts):

(d) Manuscripts

Received		Paper
08/09/2012	1.00	Stefan Mastel , Sarah Grefe , Brendan Cross , Andrew Taber, Stefano Cabrini , James Schuck , Yohannes Abate. Real-Space Mapping of Nanoplasmonic Hotspots via Optical Antenna-Gap Loading, Appl. Phys. Lett. (07 2012)
08/29/2013	3.00	Shahab Derakhshan, , Yohannes Abate, Sarah Elaine Grefe, . Near-field Nanoscale Investigation of Optical Properties of Bi2Se3 Thin-films, MRS Proceedings (08 2013)
08/29/2013	4.00	Phuong-Hieu T. Nguyen,, Farshid Ramezanipour,, John E. Greedan,, Lachlan M. D. Cranswick,, Shahab Derakhshan. Synthesis, Crystal Structure, and Magnetic Properties of Li3Mg2OsO6,a Geometrically Frustrated Osmium(V) Oxide with an Ordered RockSalt Structure: Comparison with Isostructural Li3Mg2RuO6, Inorganic Chemistry (10 2012)
08/29/2013	6.00	Xiaobo Yin, , Arun Majumdar, , Xiang Zhang, Jia Zhu, , Kedar Hippalgaonkar,, Sheng Shen, Yohannes Abate, , Kevin Wang, Sangwook Lee, , Junqiao Wu,. Temperature Gated Thermal Rectifier for Active Heat Flow Control, Nature (Submitted) (10 2013)
08/29/2013	2.00	Sarah E. Grefe, Daan Leiva, Yohannes Abate, Stefan Mastel, Scott D. Dhuey, Stefano Cabrini, P. James Schuck. Near-field spatial mapping of strongly interacting multiple plasmonic infrared antennas, Physical Chem Chem Physics (08 2013)
12/30/2015	20.00	Yohannes Abate, Sampath Gamage, Li Zhen, Stephen B. Cronin, Han Wang, Viktoriia Babicheva, Mohammad H. Javani, Mark I. Stockman. Nanoscopy Reveals Metallic Black Phosphorus, ArXive-prints, 2015 (06 2015)
12/30/2015	22.00	David Russell,, Abbey Nee,, Brent Melot,, Shahab Derakhshan. Long Range Antiferromagnetic ordering in B-site Ordered Double Perovskite; Ca2ScOsO6, Inorganic Chemistry (11 2015)
12/30/2015	23.00	Phoung-Hieu T Nguyen,, Moureen C Kemei,, Malinda S Tan,, Shahab Derakhshan. Synthesis, Crystal Structure and Magnetic Properties of the Two Polymorphs of Novel S =1 Osmate; Li4MgOsO6, Journal of Solid State Chemistry (11 2015)

TOTAL: **8**

Number of Manuscripts:

Books

Received	Book

TOTAL:

Received		Book Chapter
08/29/2013	5.00	YOHANNES ABATE. Near-field Spectroscopy and Imaging of Single Nanoparticles, Dekker Encyclopedia of Nanoscience and Nanotechnology: Taylor & Francis Group, (01 2014)
08/29/2014	12.00	Yohannes Abate. Near-Field Spectroscopy and Imaging of Single Nanoparticles, Dekker Encyclopedia of Nanoscience and Nanotechnology, Third Edition: Taylor & Francis Group, (01 2014)

TOTAL: **2**

Patents Submitted

Patents Awarded

Awards

Derakhshan:

• CNSM Faculty Award for Excellence, Pretty Darn Good Professor Award, Fall 2014.
• Faculty Research, Scholarship and Creative Activities (RSCA), institutional, Spring 2015.
• CNSM-Academic Affairs Student Success Award, Fall 2013.
• Faculty Research, Scholarship and Creative Activities (RSCA), institutional, Fall 2014.
• Research Stimulation Award, Scholarship and Creative Activities (RSCA), institutional, Spring 2014.
• CSULB Multidisciplinary Research Award.
• Faculty Research, Scholarship and Creative Activities (RSCA), institutional, Spring 2014.
• CSULB Faculty small grant. 2015

Abate:

• Most Valuable Professor, California State University Long Beach Alumni Association, Springl 2014.
• Faculty Research, Scholarship and Creative Activities (RSCA), institutional, Spring 2014.
• Research Stimulation Award, Scholarship and Creative Activities (RSCA), institutional, Fall 2014.
• CSULB Multidisciplinary Research Award.

Abate:
• Scialog Collaborative Innovative Award, Research Corporation for Science Advancement (RSCA), Spring 2015

Graduate Students

NAME	PERCENT_SUPPORTED	Discipline
Sarah Grefe	0.30	
Terry Dunlop	0.20	
Raul Torrico	0.20	
Ralph Damatto	0.20	
William Hutzel	0.10	
Luis Leal	0.10	
Andrea Citati	0.10	
Bredan Cross	0.10	
Cheryl Sturm	0.10	
Phoung Hieu Nguyen	0.10	
FTE Equivalent:	**1.50**	
Total Number:	**10**	

Names of Post Doctorates

NAME	PERCENT_SUPPORTED
FTE Equivalent:	
Total Number:	

Names of Faculty Supported

NAME	PERCENT_SUPPORTED	National Academy Member
Shahab Derakhshan	0.20	No
Yohannes Abate	0.20	
FTE Equivalent:	**0.40**	
Total Number:	**2**	

Names of Under Graduate students supported

NAME	PERCENT_SUPPORTED	Discipline
Ryan Clark	0.10	Chemistry
Phuong Hiue Nguyen	0.10	Biochemistry
Kelly Vineyard	0.10	Chemistry
Joseph Swabeck	0.10	Chemistry
Charles Bloed	0.10	Chemistry
Malinda Tan	0.10	Biochemistry
Fady Kilada	0.10	Chemistry
Erica Handley	0.10	Chemistry
Sarah Zhu	0.10	Chemistry
Stephanie Ariza	0.10	Chemistry
Katrina Bautista	0.10	Chemistry
Stephanie Sodergren	0.10	physics
Jill Pestana	0.10	physics
Brandon Hessler	0.10	physics
FTE Equivalent:	**1.40**	
Total Number:	**14**	

Student Metrics

This section only applies to graduating undergraduates supported by this agreement in this reporting period

The number of undergraduates funded by this agreement who graduated during this period: 11.00

The number of undergraduates funded by this agreement who graduated during this period with a degree in science, mathematics, engineering, or technology fields:..... 11.00

The number of undergraduates funded by your agreement who graduated during this period and will continue to pursue a graduate or Ph.D. degree in science, mathematics, engineering, or technology fields:..... 6.00

Number of graduating undergraduates who achieved a 3.5 GPA to 4.0 (4.0 max scale):..... 5.00

Number of graduating undergraduates funded by a DoD funded Center of Excellence grant for Education, Research and Engineering:..... 0.00

The number of undergraduates funded by your agreement who graduated during this period and intend to work for the Department of Defense 1.00

The number of undergraduates funded by your agreement who graduated during this period and will receive scholarships or fellowships for further studies in science, mathematics, engineering or technology fields:..... 6.00

Names of Personnel receiving masters degrees

NAME
Phuong Hiue Nguyen
Cheryl Sturm
Sarah Grefe
Raul TOrrico
Terry Dunlop
Ralph Damatto
Total Number: 6

Names of personnel receiving PHDs

NAME
Total Number:

Names of other research staff

NAME	PERCENT_SUPPORTED
FTE Equivalent:	
Total Number:	

Sub Contractors (DD882)

1 a. Georgia State University

1 b. University Plaza
P.O. Box 3999
Atlanta GA 303023999

Sub Contractor Numbers (c): SP00011843
Patent Clause Number (d-1):
Patent Date (d-2):
Work Description (e): Due to the relocation of the former PI Dr. Abate to GSU he continued the work in his new
Sub Contract Award Date (f-1): 8/16/14 12:00AM
Sub Contract Est Completion Date(f-2): 9/30/15 12:00AM

---

1 a. Georgia State University

1 b. University Plaza
P.O. Box 3999
Atlanta GA 303023999

Sub Contractor Numbers (c): SP00011843
Patent Clause Number (d-1):
Patent Date (d-2):
Work Description (e): Due to the relocation of the former PI Dr. Abate to GSU he continued the work in his new
Sub Contract Award Date (f-1): 8/16/14 12:00AM
Sub Contract Est Completion Date(f-2): 9/30/15 12:00AM

Inventions (DD882)

Scientific Progress

Technology Transfer

Final Scientific Progress Report

Near-field Nanoscopy of Metal-Insulator Phase Transitions Towards Synthesis of Novel Correlated Transition Metal Oxides and Their Interaction with Plasmon Resonances

W911NF-12-1-0076

Shahab Derakhshan, PhD
Associate professor
Department of Chemistry and Biochemistry
California State University Long Beach

Yohannes Abate, PhD
Assistant professor
Department of Physics and Astronomy
California State University Long Beach
and
Georgia State University (since July 2014)

Table of contents

Near-field nanoscale imaging of tapered suspended VO_2 crystal beams	3
Near-field Nanoscopy of Metal-Insulator Phase Transitions Correlated Transition Metal Oxides and Their Interaction with Plasmon Resonances	7
Near-field Nanoscale Investigation of Optical Properties of topological phases of Bi_2Se_3 Thin-films	9
Control of Plasmonic Nanoantennas by Reversible Metal-Insulator Transition	10
Nanoscopy of Phase Transition in VO_2 Crystals and Plasmons in Au Antennas	13
Nanoscopy Reveals Surface-Metallic Black Phosphorus	15
Synthesis, Crystal Structure and Magnetic Properties of $Li_3Mg_2OsO_6$, a Geometrically Frustrated Osmium (V) Oxide with an Ordered Rock Salt Structure: Comparison with Isostructural $Li_3Mg_2RuO_6$	19
Structure Variations and Magnetic Properties of Two Novel Osmate Polymorphs with Li_4MgOsO_6 Chemical Composition	21
Ferrimagnetism in Honeycomb Lattices of Novel Osmates; Li_4NiOsO_6 and $Li_3Ni_2OsO_6$	25
Long Range Antiferromagnetic Transition in Novel B-site Ordered Double Perovskite Ca_2ScOsO_6	27
Partial Spin Ordering and Complex Magnetic Structure in $BaYFeO_4$: A Neutron Diffraction and High Temperature Susceptibility Study	29
$CaYGaO_4$; a Fully Ordered Novel Olivine Type Gallate	32
Synthesis, Crystal Structure and Physical Properties of $La_3Al_{1-x}Si_xCuQ_7$ (Q =S, Se)	34
References	36
Summary	38

Near-field nanoscale imaging of tapered suspended VO_2 crystal beams

We employed scattering type scanning near-field optical microscope (s-SNOM) to probe the possible existence of mixed phases. S-SNOM allows direct imaging of evolution of insulating and metallic phases with increasing temperature at nanometer-scale spatial resolution. A linearly polarized probing CO_2 laser (wavelength, λ=10.7 μm) is focused on the tip-sample interface, high harmonic demodulation coupled with pseudo-heterodyne interferometer are used to detect the near-field signal with ~30nm spatial resolution above the tapered VO_2 beam.[1] The image contrast is determined by the local spatially varying dielectric function of the surface. Hence, regions of the metallic phase, due to larger effective tip-sample polarizability, result in higher s-SNOM amplitude signal compared with that of the insulating phase. The wavelength of the laser was chosen specifically in order to maximize the difference in the optical conductivity of the insulating and metallic phases of VO_2 and thus achieve optimum s-SNOM amplitude contrast at different temperatures. Interestingly, for a tapered beam demonstrating ~15% thermal rectification at 300K, there exists s-SNOM amplitude contrast across the taper confirming phase coexistence at the same temperature, which disappears when the sample is heated up to 350K. A similar experiment on a uniform cross-section beam shows no amplitude contrast evolution.

Near-field infrared spectroscopic imaging was performed with (scattering type scanning near-field microscope (s-SNOM) which is based on a tapping mode AFM.[2] Vertically vibrating PtIr-coated Si-tip (apex radius R ≈ 20 nm) with an amplitude of about 25-30 nm at a frequency of $\Omega \approx 280$ kHz is illuminated by a focused CO_2 laser beam at wavelength, λ=10.7 μm. The tip converts the illuminating radiation diffraction limited spot into a highly localized and enhanced near field at the tip apex. Due to the near-field interaction between tip and sample, the back-scattered radiation from the probe tip is modified in both amplitude and phase, commensurate to the local dielectric response of the sample. The tip-scattered light is detected using a pseudo-heterodyne interferometric detection scheme, which enables simultaneous recording of amplitude and phase of the scattered field. Background signals are efficiently suppressed by

demodulating the detector signal at the second harmonic of the tip oscillating frequency.

The contrast formation in s-SNOM near-field imaging of metal-insulator transition (MIT) in VO_2 is understood by considering the scattered signal at the second harmonic of the tip frequency as a function of the optical constants of the tip and the sample.[3] Metallic regions show higher scattering amplitude owing to large negative real part and large positive imaginary part of the optical constants at λ=10.7 μm. Insulating regions have lower scattering amplitudes because of the small imaginary and real part of the optical constants. This difference in locally varying optical constants, and thus s-SNOM scattering amplitude signal, provides the basis for image contrast formation of MIT in VO_2. As a result of stress induced by the substrate the crystal displays periodic metallic and insulating domains that are generated during the MIT. The spatial periodic variation of dielectric function of the surface results in periodic set of insulating and metallic domain image contrast due to convoluted effective polarizability of tip and sample. Metallic regions possess larger optical constants, which provide a higher effective tip-sample polarizability and thus a higher s-SNOM contrast in both amplitude and phase compared to the dielectric insulating phases. Such coexisting insulating and metallic phase in VO_2 crystal beams across MIT has been seen before both by far-field and near-field microscopy techniques.

We directly observe the nanoscale spatial evolution of one phase to another of a tapered crystal VO_2 beam grown on SiO_2. We selected to perform s-SNOM direct imaging of MIT at laser wavelength, λ=10.7 μm because the dielectric constant of the insulating and metallic phases of VO2 display significant differences at this wavelength that allow strong s-SNOM optical contrast. We find that the characteristic phase evolution is qualitatively different from a rod, the uniformly M1 structure thinner part of the taper generates brighter contrast than the wider side suggesting phase coexistence even at room temperature. As temperature is increased inhomogeneous mixed phase dynamics across the taper is observed until the phase transition is more complete at higher T leading to a more uniform bright near-field contrast.

We then consider phase evolution at MIT on a straight suspended VO_2 beams. Suspended beams offer excellent platform to investigate the spatial dynamics of the nanoscale MIT evolution without the presence of stress. Unlike a tapered beam, which displays s-SNOM amplitude contrast at room temperature, the contrast evolves uniformly across the rod displaying strong contrast in the metallic phase compared to the insulating phase. No periodic metallic and insulating domains even at phase transition temperature are observed in the near-field amplitude image, as substrate-induced stress is absent.

While the s-SNOM show unequivocally the presence of mixed phases, the origin of these remains to be ascertained. As explained above, these could be due to a variation of stoichiometry along the beam length. We also found a signature of mixed vanadium oxide phases in tapered beams using Auger Electron Spectroscopy (AES). However, recent work shows that in addition to stoichiometry, the phase transition also depends on stress fields within single VO_2 beams. It is possible that the taper created during the beam growth may lead to stress gradients which could produce geometrical and size distributions of metallic and insulating domains and interfaces near the taper. These can amplify the rectification achieved by single interfaces. Similar distributions were previous reported by bending the beam. Hence, while the metal-insulator phase transition is critical to thermal rectification, the taper and composition variation may also contribute to the effect by unique distributions of metal-insulator domains. The metal-insulator domains and interfaces can be rationally engineered to control the thermal transport. In stoichiometric VO_2 beams, an array of metal domains can be created below 340K by either substitution doping or local stressing. In addition, metal domains can be stabilized along these VO_2 beams at sub-340K temperatures by encoding stoichiometry variation during the growth or post-growth hydrogenation. Over the last several decades, while tremendous progress has been made in understanding the complexity of the metal-insulator phase transition in the family of vanadium oxides, the underlying physics still remains largely illusive. Its impact on thermal transport is much less explored and has yet to be fully understood. Rational synthesis of vanadium oxide based beams with controlled local stresses and/or stoichiometry with a lack or excess of oxygen can open up rich pathways to further manipulate heat transfer in these systems.

In summary, we report an unprecedented large thermal rectification up to 22% in VO_2 beams that is gated by the environmental temperature. It is the first demonstration of an active three-terminal thermal device exhibiting an "on" rectifying state over large range of temperature (T_G = 250-340 K) and "off" resistor state (T_G < 250 K or T_G> 340K). By changing temperature, one can switch the rectification, much like a gate voltage switches a thyristor between two states of electrical conductance. The realization of such unique thermal control is a consequence of the interplay between metallic and insulating phases due to the rich parameter space provided by the vanadium-oxygen material family. Such novel all-thermal devices may spurn interesting applications in autonomous thermal flow control and efficient energy harvesting.

Near-field Nanoscopy of Metal-Insulator Phase Transitions Correlated Transition Metal Oxides and Their Interaction with Plasmon Resonances

By designing, simulating and fabricating hybrid plasmonic/VO_2 nanostructures, we have imaged with nanoscale spatial resolution in real-space how the plasmon dipolar modes are modulated and the effect of the plasmon on the characteristic insulator-to-metal transition VO_2. We first performed polarization-selective scattering-type scanning near-field optical microscope (s-SNOM) measurements to directly visualize the dipolar near-field distributions and couplings of plasmonic triangles, bowties and cross-bowtie antennas in the mid-infrared (9-11 μm) spectral regime.[3] We systematically investigate the coupling mechanism by first imaging the near-field distribution of a single triangular Antenna. While monitoring its field distribution, we add another identical antenna closer and closer to it (essentially forming bowties of varying gap width). We then cross the existing bowtie with another bowtie (forming a cross bowtie at varying proximity distances) and monitor the evolution of the strongly coupled dipolar field distribution modified through inter-antenna charge-dipole and dipole-dipole Coulomb interactions by performing polarization control measurements. The triangular plasmonic metal nanostructures concentrate plasmons into the sharp end and smear them over the widened base, resulting in dipolar modes with higher field intensity at the sharp end, and largely suppressed field at the base. We find that the aspect ratio, base and sharp end width determine the symmetry and intensity of localized field profiles, both for single particles and particle aggregates. Employing cross-polarized S/P s-SNOM imaging scheme (exciting along the in-plane direction, S-excitation, and detecting the out-of-plane near-field component, P-detection), we further demonstrate that cross-bowtie structures could be used as active infrared polarization filters. Such devices would be of interest to realizing antenna structures for surface enhanced infrared absorption spectroscopy, to manipulate optical fields in subwavelength field distributions, plasmonic filtering and polarization selection applications.

Subsequently plasmonic structures were fabricated on VO_2 thin films using ebeam

lithography The hybrid plasmonic/VO_2 nanostructures, were then imaged in the near-field at different temperature following the percolation dynamics of the VO_2 film. By spatially confining electromagnetic fields to nanoscale volumes using nanogaps formed by metallic nanostructurewe tailor the near-field environment with a VO_2 characteristic MIT. By providing real time nanoscale optical studies of a hybrid nanomaterial, we demonstrate a novel way to manipulate the nanoscale plasmon couplings formed in metallic plasmonic structures.

Near-field Nanoscale Investigation of Optical Properties of topological phases of Bi_2Se_3 Thin-films

Among some of the most exciting discoveries in the past few years in condensed matter research is the theoretical foundations of topological insulating electronic phases based on strong spin-orbit coupling and observations of the these states in model materials. On the surface of topological insulators (TIs) such as Bi_2Se_3 the electronic spectrum is characterized by a single helical Dirac dispersion such that counter-propagating electrons carry opposite spin allowing propagation of pure spin currents. In addition to their fundamental scientific novelty, these states are predicted to have special properties arising from charge dynamics that could be driven optically, making them potentially useful for applications ranging from opto-spintronic devices, quantum computation, nanoscale electronics and nanophotonics.

Here we investigate near-field optical properties of Bi_2Se_3 thin films using spectroscopic s-SNOM.[4] Bulk Bi_2Se_3 samples were synthesized by conventional high temperature solid-state method. Formation of single phases of Bi_2Se_3 were confirmed by powder X-ray diffraction technique. Thin film Bi_2Se_3 samples were prepared by mechanical exfoliation on silicon wafers. By imaging several Bi_2Se_3 thin films with s-SNOM, we discovered size and wavelength dependent near-field contrast in both amplitude and phase. S-SNOM can directly visualize the Re(ε) of the sample's dielectric function ε in amplitude, while phase images map Im(ε). Retraction curves taken at several locations confirm that the contrasts observed were from evanescent near-field interactions. Another solution to the possible contamination from exfoliation techniques is also to eliminate tape altogether. We introduce a "shear exfoliation" sample preparation method, which reliably deposits Bi_2Se_3 and Bi_2Te_3 without the possibility of adhesive contaminants.

Control of Plasmonic Nanoantennas by Reversible Metal-Insulator Transition [6]

We demonstrate dynamic reversible switching of VO_2 insulator-to-metal transition (IMT) locally on the scale of 15 nm or less and control of nanoantennas, observed for the first time in the near-field. Using polarization-selective near-field imaging techniques, we simultaneously monitor the IMT in VO_2 and the change of plasmons on gold infrared nanoantennas. Structured nanodomains of the metallic VO_2 locally and reversibly transform infrared plasmonic dipole nanoantennas to monopole nanoantennas. Fundamentally, the IMT in VO_2 can be triggered on femtosecond timescale to allow ultrafast nanoscale control of optical phenomena. These unique features open up promising novel applications in active nanophotonics.

In this work, we demonstrate unprecedented active nanoscale control of concentration of light by single plasmonic infrared antennas in the near-field. The active control of the dielectric environment by the insulator-to-metal transition (IMT) in vanadium oxide (VO_2), dynamically the transforms nanoantennas from dipole to monopole and back. We utilize the local, reversible change of refractive index of VO_2 that undergoes a first-order phase transition from an insulating monoclinic phase to a metallic rutile phase near 70 °C in bulk single crystals14, the transition can also be induced by strain and ultrafast light pulses. In polycrystalline VO_2 thin films, the IMT begins as conductive nanodomains nucleate and with increasing temperature evolve to interconnect in a percolative fashion throughout the film19. At intermediate stages of the IMT, insulating and metallic phases coexist, forming a network of highand low-conductivity nanodomains throughout the film. Since the metallic and insulating nanodomains have substantially different refractive indices, VO_2 films provide for direct local control of the dielectric environment at nanometer spatial dimensions, which, in turn, can directly modulate optical responses of nanophotonic structures.

Near-field infrared spectroscopic imaging was performed with (scattering type scanning near-field microscope (s-SNOM) which is based on a tapping mode AFM. Vertically vibrating PtIr-coated Si-tip (apex radius $R \approx 20$ nm) with an amplitude of about 25-30 nm at a frequency of $\Omega \approx 280$ kHz is illuminated by a focused CO_2 laser

beam at wavelength, λ=10.7 μm. The tip converts the illuminating radiation diffraction limited spot into a highly localized and enhanced near field at the tip apex. Due to the near-field interaction between tip and sample, the back-scattered radiation from the probe tip is modified in both amplitude and phase, commensurate to the local dielectric response of the sample. The tip-scattered light is detected using a pseudo-heterodyne interferometric detection scheme, which enables simultaneous recording of amplitude and phase of the scattered field. Background signals are efficiently suppressed by demodulating the detector signal at the second harmonic of the tip oscillating frequency.

To directly visualize plasmonic modes of the antennas and their interaction with the IMT of the VO_2 film, we implement in-plane polarization-selective excitation (s-excitation, i.e. polarized along the y direction) and in-plane detection (s-detection), which is referred to s/s imaging. Figure 1 shows topography, third-harmonic s/s near-field amplitudes, and phase images of the antennas on the VO_2 film for different temperatures. The four IR antennas are nominally identical (Figure 1a), making it possible to compare the effects of VO_2 IMT on them. The amplitude images (Figure 1b–d) show bright and dark optical contrast due to the coexisting insulating (dark) and metallic (bright) phases affecting the nanoscale dielectric environment of the antennas. The metallic phase begins to form randomly with increasing temperature. As a result, portions of the antennas are located partly on the metallic and partly on the insulating phases of VO_2 as observed in the amplitude images (Figure 1b–d). The amplitude images allow one to see the change of nanoscale field magnitudes and the metallic phase formation . At the same time, the near-field phase images e–h are less sensitive to material contrast but allow one to follow the dipolar mode modification on each of the four antennas due to IMT. They display strong phase contrast at the rod ends. The VO_2 regions exhibit very weak phase contrast as shown in Figure 1e–h, which is independent of excitation or detection polarizations.

At room temperature, all antennas display identically the expected pronounced dipolar phase contrast at their ends, as shown in Figure 1e. At higher temperatures, all antennas whose one end is situated on the metallic phase turn from dipole to monopole as evident for Rod 1 (Figure 1f–h), Rod 3 (Figure 1f), and Rod 4 (Figure 1f–g). At even higher temperature, when the amplitude image shows that most of the film is in metallic

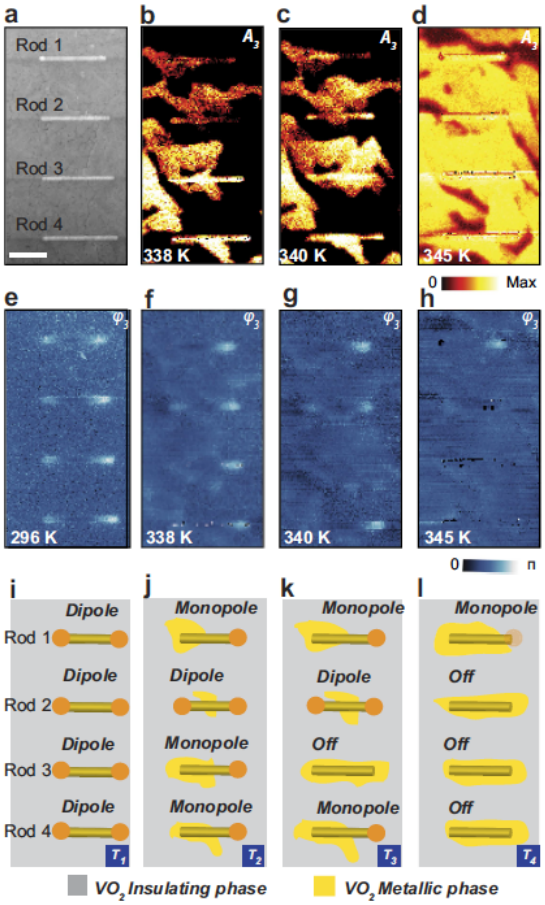

Figure 1. Temperature-controlled IMT and antenna near-field images. Near-field 3rd harmonic amplitude (b–d) and phase (e–h) images.

Schematics (i–l) describing experimental results of IR plasmonic antenna modes simultaneously with VO_2 thin film IMT domain formation and propagation.

phase (Figure 1d), both dipole and monopole antenna modes of Rods 2, 3 and 4 turn off (Figure 1h) completely. An interesting case is Rod 2: despite the middle part of the rod sitting on the metallic phase (Figure 1c), it still retains its dipole characteristics (Figure 1g) since both ends are on the insulating grains. It only turns off at higher temperature when the entire antenna is situated on metal (Figure 1h). These results are interpreted in schematics shown in Figure 1i–l. The summary of this work is the first experimental evidence that near-field local optical processes in plasmonic nanostructures can be directly and actively controlled by nanodomains in VO_2 film as it undergoes the IMT. Depending on the precise location of the nanoantennas with respect to metallic and insulating domains in the VO_2 film on the scale of 15 nm or less, the IMT reversibly transforms infrared plasmonic dipole antennas to monopole antennas or switches them off. We envision that such dynamic active control of the nanoscale interaction of light with nanostructured materials, which can potentially be ultrafast, will open up diverse applications in nanooptics and the related technologies.

Nanoscopy of Phase Transition in VO_2 Crystals and Plasmons in Au Antennas

We investigate vanadium dioxide (VO_2) bulk crystals for nanoplasmonics local manipulation using high-resolution nanoscopy. We examined various types of VO_2 crystals such as strained ones grown on sapphire substrate, free-standing pure VO_2 crystals and tungsten doped suspended VO_2 crystals. Strained crystal beams provide better control of metal (M) insulator (I) phases with sharp transitions that offer excellent opportunity for switching and manipulation of plasmons. Compared to thin film VO_2 samples, the crystal beams generate quasi-reproducible, uniform M and I regions separated by a sharp interface as confirmed by nanoimaging. The periodic stripes are caused by strain due to the substrate, such stripes are absent in both free-standing and tungsten doped VO_2 crystals. We used these periodic stripes in strained VO_2 to manipulate plasmon hot spots in Au infrared antennas fabricated on the crystal at different orientation with respect to the excitation laser. The M-I transition in VO_2 is not affected by the antenna plasmons as such, the antennas serve as a good reporter of the phase transition.

In this work we compare several types of VO_2 samples such as strained signle crystals, free-standing pure and tungsten doped VO_2 crystals and films for nanophotonics local manipulation. The crystal provides non-percolative and ultrafast switching of metal insulator phases with a sharp transition MIT good for switching compared to polycrystal films investigated. We study the near-field MIT evolution using scattering type scanning near-field optical microscope (s-SNOM) in these samples and demonstrate plasmon switching using the MIT. In strained crystals, periodic M-I stripes are observed which are absent in identical but free-standing VO_2 crystal beams. In graded-tungsten doped VO_2 crystals, M-I phase separation is already evident even at room temperature and as temperature is increased the interface evolves until the crystal becomes uniformly metallic. [7] Since the strained VO_2 crystals on substrate provide evident contrast between the mixed phases, we then used the periodic M-I stripes to fabricate local gold (Au) nanorods and manipulate plasmon hot spots, **Fig. 1**. Further, by orienting Au plasmonic antenna rods on VO_2 crystals at different angles with respect to the excitation laser and

studying their near-field optical signal with high resolution shows evolution of the dipolar mode at room temperature and reversible on and off dipolar modes during MIT of the crystal (**Fig. 1**).

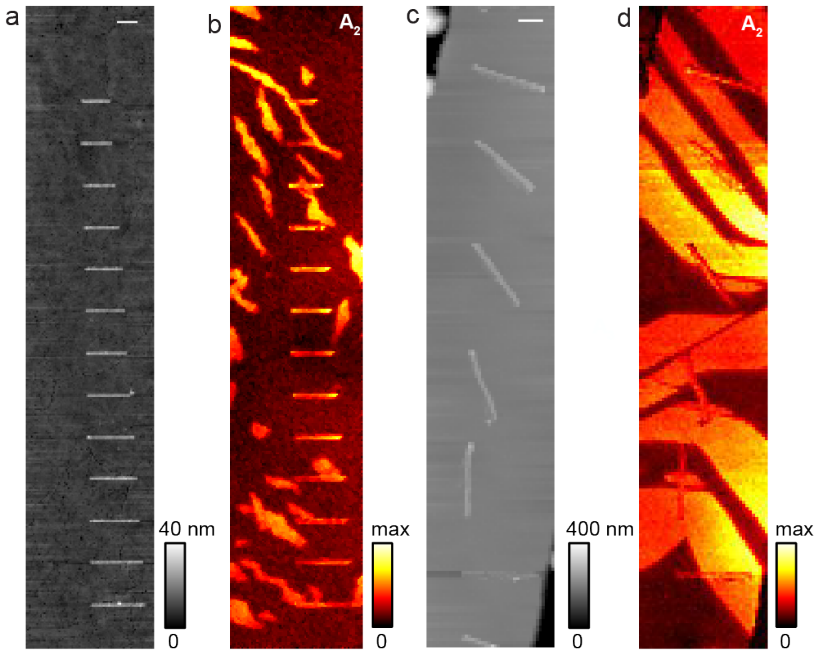

Fig. 1. S-SNOM Topography (a) and second harmonic near-field amplitude (b) images of a Au antennas fabricated on VO_2 film deposited on Si substrate imaged at T~67^{0}C. The topography (c) and near-field amplitude (d) images of Au rods fabricated on single crystal VO_2 beams grown on sapphire substrate also imaged at T~73^{0}C. All near-field images are recorded at laser wavelength, λ=10.7 μm.

Nanoscopy Reveals Surface-Metallic Black Phosphorus [8]

Nanolayer and two-dimensional (2D) materials [9] such as grapheme [10, 11], boron nitride [9, 12], transition metal dichalcogenides [9, 13-16] (TMDCs), and black phosphorus (BP) [9, 17-21] have intriguing fundamental physical properties and bear promise of important applications in electronics and optics [17, 22, 23]. Of them, BP [19, 20, 24] is a novel layered material that has been theoretically predicted [18] to acquire plasmonic behavior for frequencies below ~0.4 eV when highly doped. The electronic properties of BP are unique due to its anisotropic structure. Advantages of BP as a material for nanoelectronics and nanooptics are due to the fact that, in contrast to metals, the free carrier density in it can be dynamically controlled by chemical or electrostatic gating, which has been demonstrated by its use in field-effect transistors.[17, 22, 23] Despite all the interest that BP attracts, near-field and plasmonic properties of BP have not yet been investigated experimentally. Here we report the first observation of nanoscopic near-field properties of BP. We have discovered near-field patterns of outside bright fringes and high surface polarizability of nanofilm BP consistent with its surface-metallic, plasmonic behavior at mid-infrared (mid-IR) frequencies below critical frequency $\omega_m \approx 1176$ cm^{-1}. This has allowed us to estimate plasma frequency $\omega_p \approx 0.4$ eV, carrier density $n \approx 1.1 \times 10^{11}$ cm^{-1} and the thickness of the surface metallic layer of ~ 1 nm. We have also observed similar behavior in other nanolayer semiconductors such as TMDC MoS_2 and topological insulator Bi_2Te_3 but not in insulators such as boron nitride. This new phenomenon is attributed to surface band-bending and charging of the semiconductor nanofilms. The surface plasmonic behavior has been found for 10-40 nm BP thickness but absent for 4 nm BP thickness. This discovery opens up a new field of research and potential applications in nanoelectronics, plasmonics, and optoelectronics.

In this work, we report the first experimental near-field optical nanoscopic investigation of BP at mid-IR frequencies. We have observed near-field amplitude patterns, which allow direct imaging of the gap field at the tip-sample junction via bright fringes formed at BP edges outside of the BP geometric boundaries. In comparison with full electrodynamic modeling, we attribute them to a high surface polarizability of BP consistent with surface-metallic, plasmonic behavior at mid-IR frequencies. Note that

such surface charging is a well-known phenomenon for conventional 3D semiconductors [25] but has never been previously reported for BP or other nanolayer materials.

Near-field optical images were acquired using a commercial s-SNOM system (neaspec.com) represented schematically in Figure 3a. A linearly polarized mid-IR quantum cascade laser (Daylight Solutions) is focused on the tip–sample interface at an angle of 45^0 to the sample surface, and the scattered field is detected by phase-modulation interferometry. Topography (Figure 3c) and third harmonic near-field amplitude images of a wedge-shaped uncoated BP exfoliated flake on a Si/SiO_2 substrate are shown at two frequencies (Figure 3d, e). Near-field amplitude images displayed in Figure 3d,e show bright contrast compared to the substrate. The amplitude image taken at ω =934.6 cm^{-1} (**Error! Reference source not found.**d) shows a bright fringe surrounding the wedge separated by a dark contrast from the inner bright surface of the structure. Such an edge fringe is missing in the near-field amplitude image taken at ω =1818.2 cm^{-1} (Figure 3e), suggesting a strong frequency dependence of the fringe formation. In fact, the fringe disappears at a critical frequency $\omega_m \approx 1176$ cm^{-1}. The observed fringe in Figure 3d is situated strictly outside the geometric limits of the BP structure as shown by the broken straight line drawn across the line profile plots of the three images shown in Figure 3b. Similar outside bright fringes followed by a dark contrast fringe are seen in Figure 3g for BP coated with 1 nm Al_2O_3 and on uncoated BP of the identical thickness (Figure 3f). We associate this outside fringe around the nano-flake of BP with high surface polarizability related to its metallic, plasmonic behavior. [After contents of this article was posted as a preprint [26] and initially submitted for a journal publication, we became aware about publication [27] where metal nanolayer at the surface of BP was observed by angular-resolved photoelectron spectroscopy (ARPES), which independently supports the present findings]. In our case, the frequency $\omega_m \approx 1176$ cm^{-1} at which the fringe disappears is the surface plasmon frequency, which corresponds the dielectric permittivity [28] $\varepsilon_{SP} = -1$. We will use the Drude formula, $\varepsilon = \varepsilon_0 - (\omega_p / \omega)^2$, where ω_p is the bulk plasma frequency of the surface layer, and ε_0 is the background (high-frequency permittivity. Setting $\varepsilon_0 = 6$ as typical for narrow-band

semiconductors, we can find $\omega_p = \omega_m \sqrt{\varepsilon_0 - \varepsilon_{SP}} \approx 0.4\ \text{eV} \approx 3224\,\text{cm}^{-1}$. From this, we find the three-dimensional electron density, $n = m_e \omega_p^2 / \left(4\pi e^2\right) \approx 1.1 \times 10^{20}\,\text{cm}^{-1}$, where e is unit charge, and m_e is electron mass, which is a density reasonable for highly-doped, conducting semiconductors exhibiting plasmonic behavior.[24] These high-density charges are likely to originate from the band bending caused by the surface dopants, as known for conventional 3D semiconductors.[20] Such charges form a surface "metallic" layer whose thickness can be estimated as the corresponding Thomas-Fermi screening length, $r_{TF} = \hbar \varepsilon_{BP}^{1/2} (2e)^{-1} m_e^{-1/2} (3n/\pi)^{-1/6} \sim 1\,\text{nm}$, where ε_{BP} is bulk permittivity of BP (we set $\varepsilon_{BP} = 6$ the same as ε_0 above).

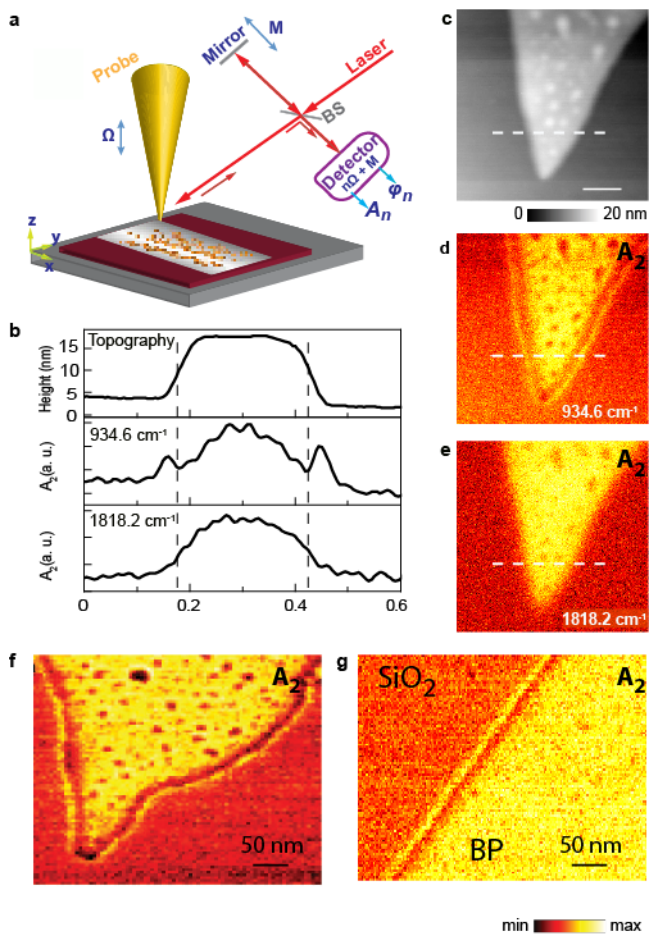

Figure 3. Edge fringe nanoscopy. (a) Experimental schematics, (b) line profiles where the broken line represents the physical boundaries of BP, (c) topography, (d) near-field amplitude images of uncoated BP at two frequencies ω = 934.6 cm^{-1}, which shows bright contrast enclosing BP the edge, (e) ω = 1818.2 cm^{-1} showing absence of the fringe. (f) Similar thickness bare BP and (g) 1-nm sapphire-coated BP. Small dark spots in uncoated samples [panels (c)-(f)] result from degradation (oxidation) of BP.

Synthesis, Crystal Structure and Magnetic Properties of $Li_3Mg_2OsO_6$, a Geometrically Frustrated Osmium (V) Oxide with an Ordered Rock Salt Structure: Comparison with Isostructural $Li_3Mg_2RuO_6$ [30]

We reported on the novel Os-based compound $Li_3Mg_2OsO_6$, which is isostructural and isoelectronic to the above-mentioned ruthenate. $Li_3Mg_2OsO_6$, was synthesized in polycrystalline form by reducing Li_5OsO_6 [31] by osmium metal and osmium (IV) oxide in the presence of stoichiometric amounts of magnesium oxide. The crystal structure was refined using powder X-ray diffraction data in the orthorhombic *Fddd* space group with a = 5.88982 (5) Å, b = 8.46873 (6) Å and c = 17.6825 (2) Å. This compound is isostructural and isoelectronic with the Ru-based system $Li_3Mg_2RuO_6$. [32] While there is no significant difference between the crystal structures of the systems, the magnetic properties of the Os phase differ markedly from those of the Ru material (Figure 4). Below the paramagnetic regime there are three anomalies at 75K, 30K and 10K. Those at 75K and 30K are suggestive of short-range AFM correlations, while that at 10K is a somewhat sharper maximum showing a ZFC/FC divergence suggestive of perhaps spin freezing. On the other hand, the ruthenate shows long-range AFM order below 17K without any other unusual feature at higher temperatures and is less frustrated, $f = 6$. [32]

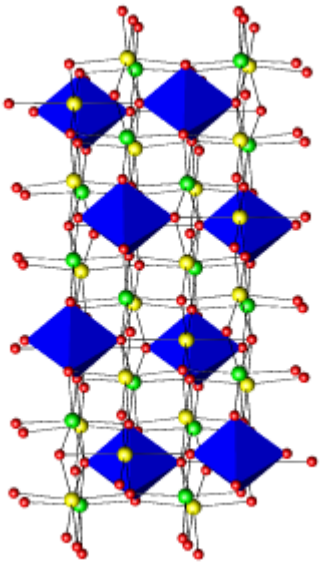

Figure 4. The crystal structure of $Li_3Mg_2MO_6$ (M = Ru, Os). The blue octahedral represent $[MO_6]^{7-}$, the yellow circles are Li rich positions and the large green circles are magnesium rich positions

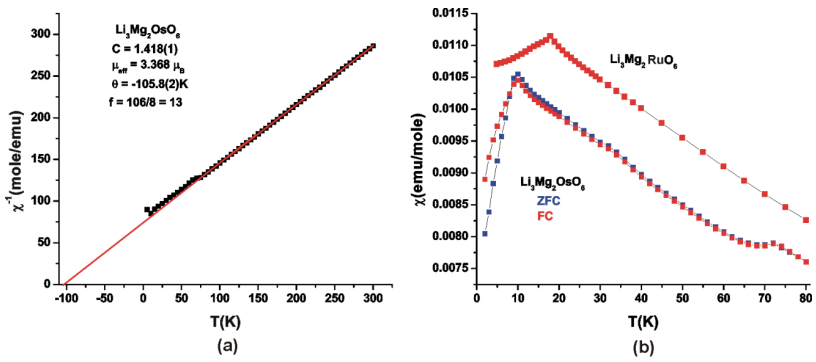

Figure 5. A Curie Weiss fit in the paramagnetic region with temperature dependent zero-field/field cooled magnetic susceptibility data and field dependence of magnetic moment for $Li_3Mg_2OsO_6$. (a) Curie-Weiss fit in the paramagnetic region, 100K – 300K. The black squares denote the inverse susceptibility values and the red line represents the fit. (The fitting parameters are shown on the figure and discussed in the text. (b) Temperature dependent zero-field cooled/field cooled magnetic susceptibility data for $Li_3Mg_2OsO_6$ between 2 – 80 K compared with corresponding data for $Li_3Mg_2RuO_6$

Moreover, while the sharp lambda anomaly in the temperature dependent heat capacity data of $Li_3Mg_2RuO_6$ supports the long-range order, in the heat capacity data of osmium material, a broad feature (near ~ 12K) is observed. This observation rules out long-range order (LRO) for $Li_3Mg_2OsO_6$ (Figure 6).

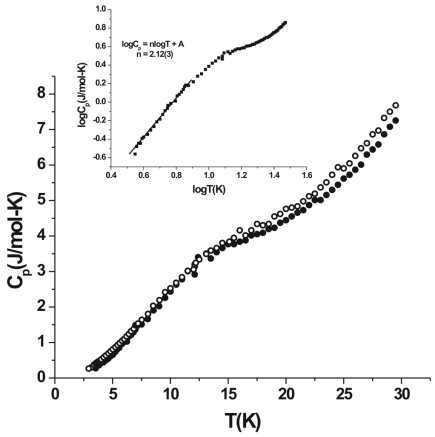

Figure 6. Heat capacity data for $Li_3Mg_2OsO_6$ at applied fields of 0T (solid circles) and 9T (open circles).

Moreover, the low temperature neutron diffraction data for the Ru compound revealed magnetic peaks (indicative of the long-range order), whereas the magnetic Bragg peaks below 10K transition for the osmium phase were absent. The inconclusive results motivated us to perform muon spin relaxation (μSR) experiments that revealed the presence of strong static magnetic order (spin frozen system) at base temperature with a clear transition at ~12K.

V. Structure Variations and Magnetic Properties Two Novel Osmates Polymorphs with Li_4MgOsO_6 Chemical Composition [33]

Prior to this work, magnetic properties of Os-based oxides in ordered rock salt were investigated for Os^{7+} and Os^{5+} systems, namely in Li_5OsO_6 [30] and $Li_3Mg_2OsO_6$, [29] respectively. In order to complete the systematic study of magnetism in these systems, attempts were devoted to prepare and study the missing Os^{6+} member, namely Li_4MgOsO_6. Preliminary data revealed that the phase is formed in more than one crystal structure types. It was noted that monoclinic *C2/m* phase is a metastable form, which converts into the orthorhombic *Fddd* structure upon longer heating period. Various methods were tried to synthesize the single-phase samples, as these systems would potentially enable to understand the role of crystal symmetry in magnetic properties of two different materials with the same chemical compositions. Pure products of Li_4MgOsO_6 in both *C2/m* and *Fddd* symmetries were obtained and confirmed by powder X-Ray Diffraction. The powder XRD pattern for two phases are represented in (Figure 7). Both polymorphs of Li_4MgOsO_6, form in ordered rock salt structure type, which comprise edge-shared octahedra. The monoclinic variant (Figure 8a) crystallizes in *C2/m* space group and is isostructural to $S = ½$ system, Li_4MgReO_6.[34] The cell constants are a = 5.1074(4) Å, b = 8.8182(4) Å, c = 5.0902(2) Å, β = 109.845(4)º, and V = 215.64(1) Å^3. Two formula units of Li_4MgOsO_6 are present in each

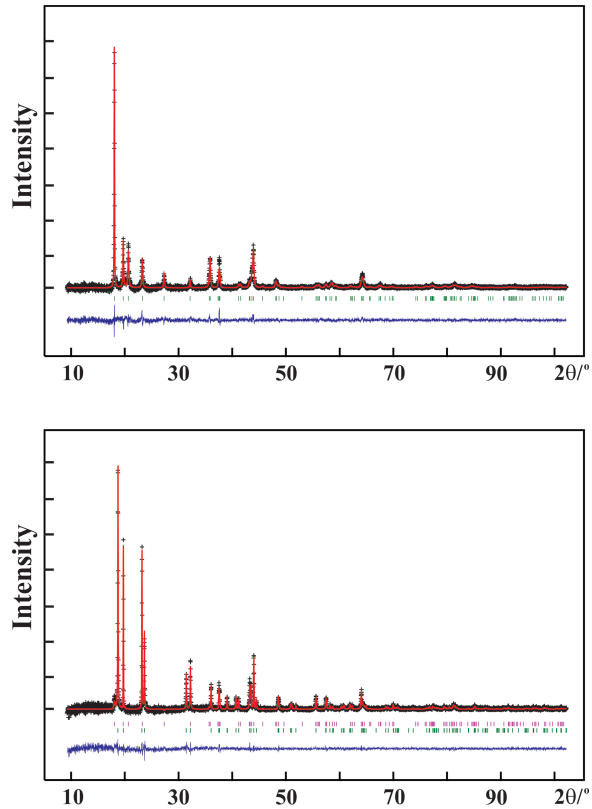

Figure 7. Room temperature powder X-ray diffraction pattern of monoclinic (top) and orthorhombic (bottom) variants of Li_4MgOsO_6. The black crosses indicate the experimental data while the Rietveld refinement fit is shown as a solid red line. The difference between these values are represented by the bottom thin blue solid line. The peak positions of the target phases are located by the green vertical tick marks and the pink vertical tick marks (bottom) represent the position of monoclinic side-product in orthorhombic sample.

unit cell. The orthorhombic system (Figure 8 b) appears in *Fddd* space group with a = 5.8485(1) Å, b = 8.3821(1) Å, c = 17.6212(3) Å and V = 863.84(2) Å^3. It is isostructural to $Li_3Mg_2RuO_6$ [32] and is composed of eight formula units per unit cell. The molar volumes of the orthorhombic phase is only 0.130(2)% larger than that of the monoclinic phase, which is indicative of nearly identical chemical compositions for the two phases. In the monoclinic crystal structure only alternate layers contain OsO_6^{6-} octahedra and these layers of magnetic ions are separated from each other along the c crystallographic axis by diamagnetic layers (edge-shared LiO_6^{-11} and MgO_6^{-10}). Except osmium positions, which are ordered in both structures, the rest of the cationic positions are mixed occupied between Li and Mg.

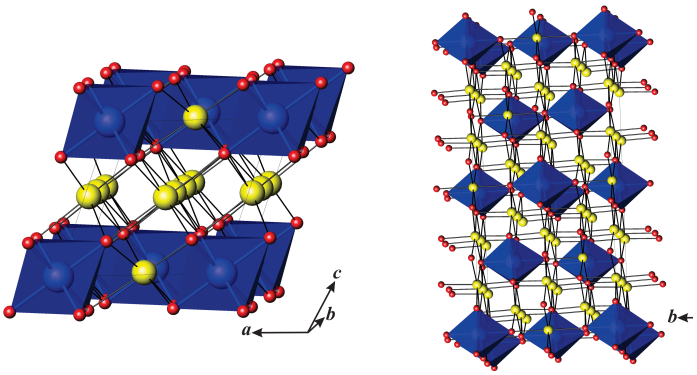

Figure 8. Crystal structure of monoclinic Li_4MgOsO_6 (left) and orthorhombic variant of Li_4MgOsO_6 (right). The blue octahedra represent OsO_6^{6-} units and the yellow spheres represent mixed occupied positions by Li^+ and Mg^{2+} ions. The red spheres represent O^{2-} anions.

Temperature dependent ZFC and FC data for both orthorhombic and the monoclinic phases of Li_4MgOsO_6 are similar in Figure 9. The Curie-Weiss fit in the paramagnetic regime, 300-380K for both phases reveal highly negative θ values, –121.87 K and –114.81 for *Fddd* and for *C2/m,* respectively. The experimental effective magnetic moment (μ_{eff}) values of 2.34 μB and 2.13 μB for both orthorhombic and monoclinic phases (respectively) are smaller than the spin only value of 2.83 μB, which are consistent with the spin-orbit coupling in the electronic configuration that are less than half filled.. Also, there is no hysteresis in the field dependence magnetic moment data at 2 K and 300 K for both phases. These measurements suggest that the transition probably happen lower than 2 K.

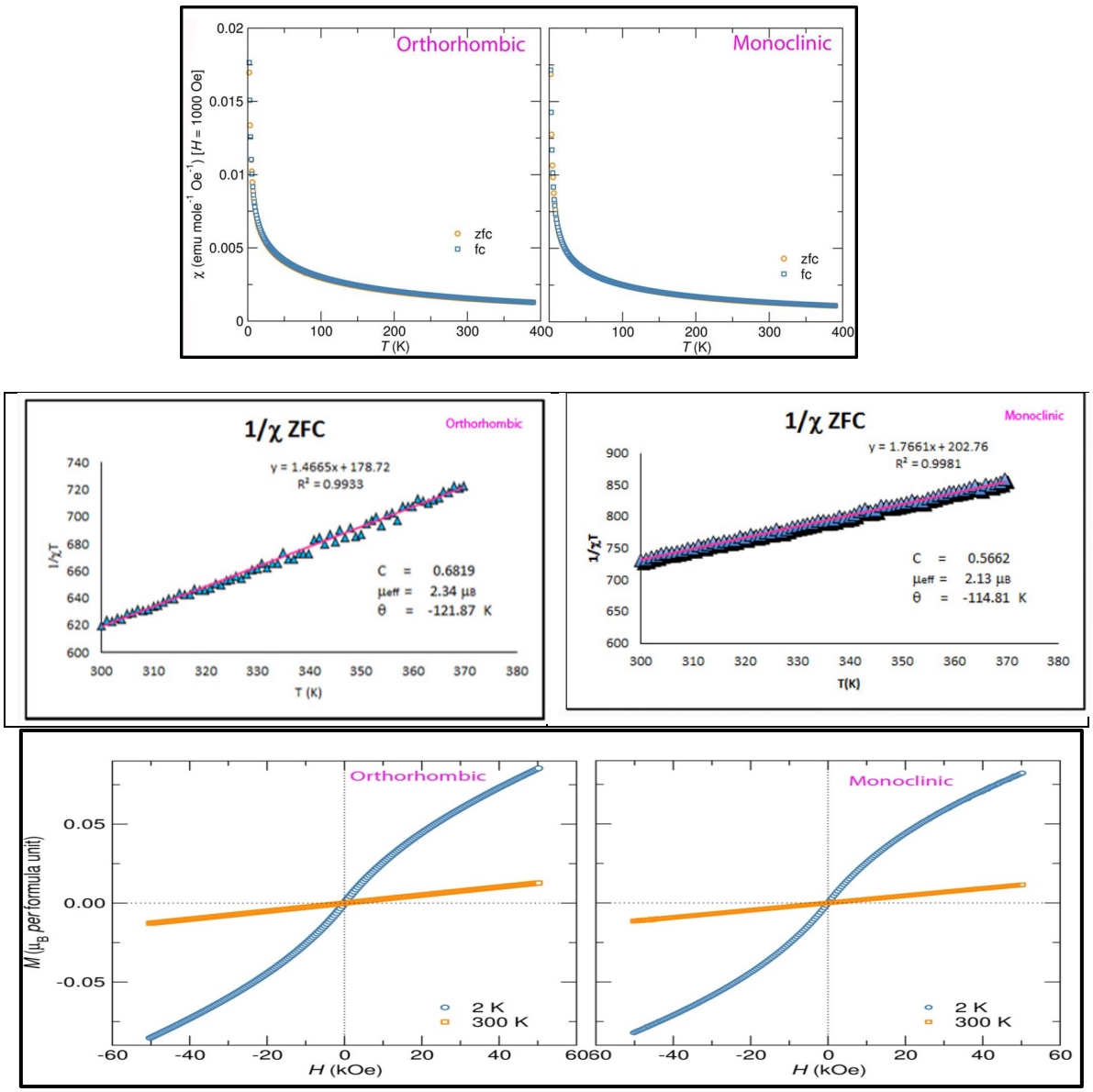

Figure 9. Temperature dependent ZFC and FC magnetic susceptibility data for the *C2/m* and *Fddd* Li_4MgOsO_6 between 0 – 400 K (top). Curie-Weiss fit in the paramagnetic region, 300K – 380K for *Fddd* and *C2/m* (middle). Field dependence of the magnetic moment for the *C2/m* and *Fddd* Li_4MgOsO_6 at 2 K and 300 K (bottom).

Even though the temperature dependent and field dependent magnetic moment data for both phases show no major difference from static magnetic properties point of view, the dynamic behavior that was monitored by relaxation technique reveal remarkable contrast. In *Fddd* system (Figure 10) there is still some magnetic responses at 5 K, which died off shortly as the temperature increased, whereas in the monoclinic system there are distinct responses at 5, 10 and 20K (Figure 11). Therefore, these novel

compounds are excellent candidates for Muon spin relaxation (μSR) study and low temperature magnetic susceptibility measurements.

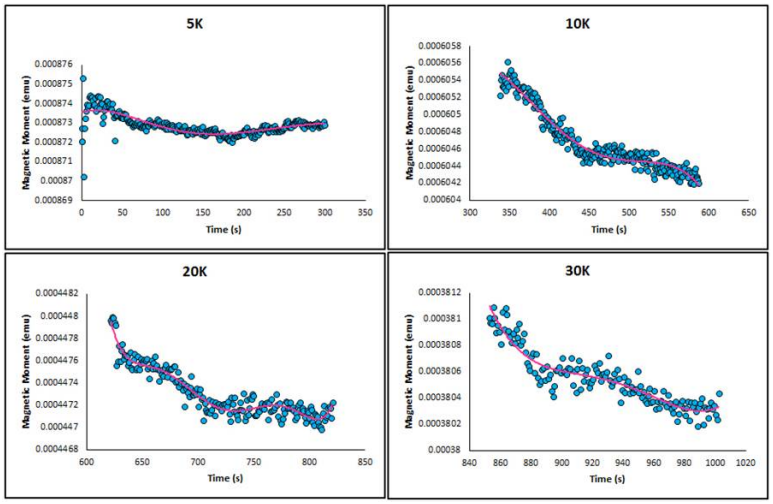

Figure 10. Magnetic relaxation measurement data for *Fddd* Li_4MgOsO_6.

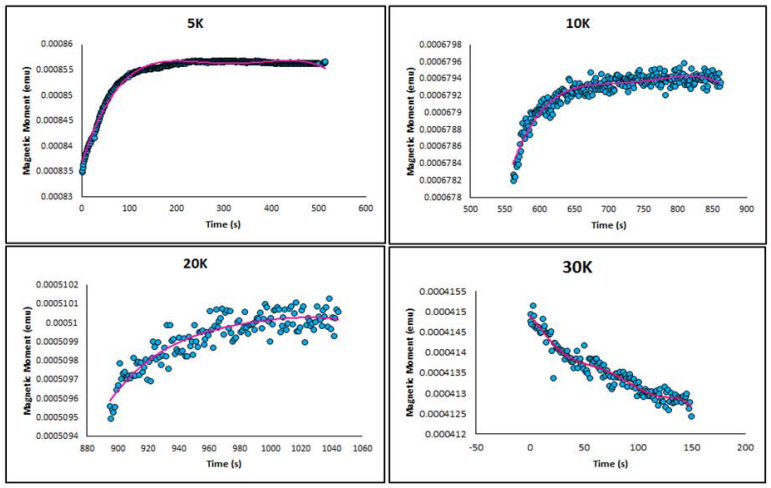

Figure 11. Magnetic relaxation measurement data for *C2/m* Li_4MgOsO_6.

Ferrimagnetism in Honeycomb Lattices of Novel Osmates; Li_4NiOsO_6 and $Li_3Ni_2OsO_6$ [35]

Two novel Osmium-based compounds Li_4NiOsO_6 and $Li_3Ni_2OsO_6$ were synthesized by solid state reaction methods. They are crystallized in the monoclinic (*C2/m*) system with the unit cell parameters of a = 5.1017 (8), b = 8.8295 (1), c = 5.0858 (6), β = 109.863 (1)◦ and V = 215.460 (3) Å^3 for the former and a = 5.1270 (1), b = 8.8582 (3), c = 5.1133 (1), β = 109.556 (2)◦ and V = 218.830 (7)Å^3 for the latter. The crystal structures are composed of quasi-2D arrangement of edge-shared octahedra forming alternate layers of Os containing honeycomb lattice (Figure 12).

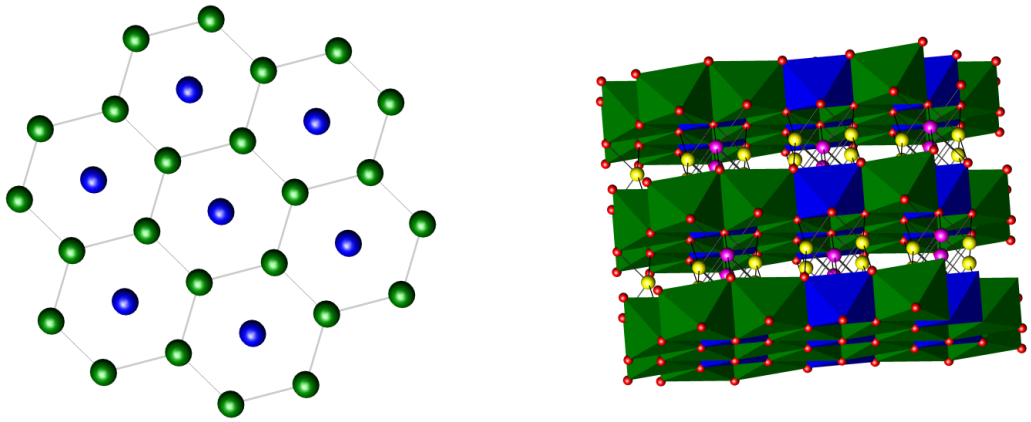

Figure 12. Honeycomb arrangement of $Li_3Ni_2OsO_6$ in *ab* plane (left) with the blue circle being osmium ion and the green is nickel. (Right) The layer of the honeycomb arrangement. Blue octahedra represent OsO_6^{7-}, which are surrounded by the green NiO_6^{10-} octahedra, the yellow circle is lithium and pink circle denotes a mixture of nickel and lithium while the red circles are oxygen.

Field dependent magnetization measurement shows hysteresis at 2 K for Li_4MgOsO_6 and 2 K, 5 K, 10 K and 15 K for Li_3Ni_2OsO suggesting ferrimagnetic ordering in the system (Figure 13 and 14).

Magnetic susceptibility data were collected from 2 K to 300 K for both compounds (Figure 15). By performing the Curie-Weiss fit, large negative θ values of -141 K for Li_4NiOsO_6 and -318 K for $Li_3Ni_2OsO_6$ reveals that the system contain two unequal opposing antiferromagnetic sublattices. They cancel each other out but not entirely resulting in the ferrimagnetic behavior in the system. The experimental effective magnetic moment (μ_{eff}) values for both $Li_3Ni_2OsO_6$ and $Li_3Ni_2OsO_6$values are 3.89 μB and 7.1 μB respectively.

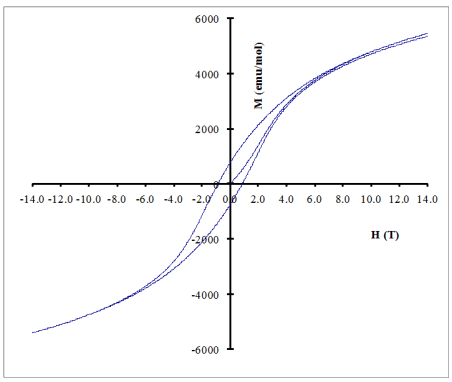

Figure 13. Field dependence of the magnetic moment for the Li_4NiOsO_6 at 2 K shows a hysteresis

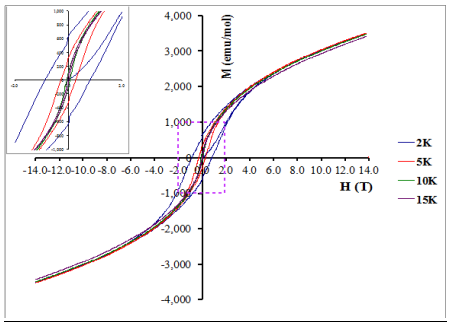

Figure 14. Field dependence of the magnetic moment for the $Li_3Ni_2OsO_6$ at 2 K, 5 K, 10 K and 15 K. All of them show hysteresis.

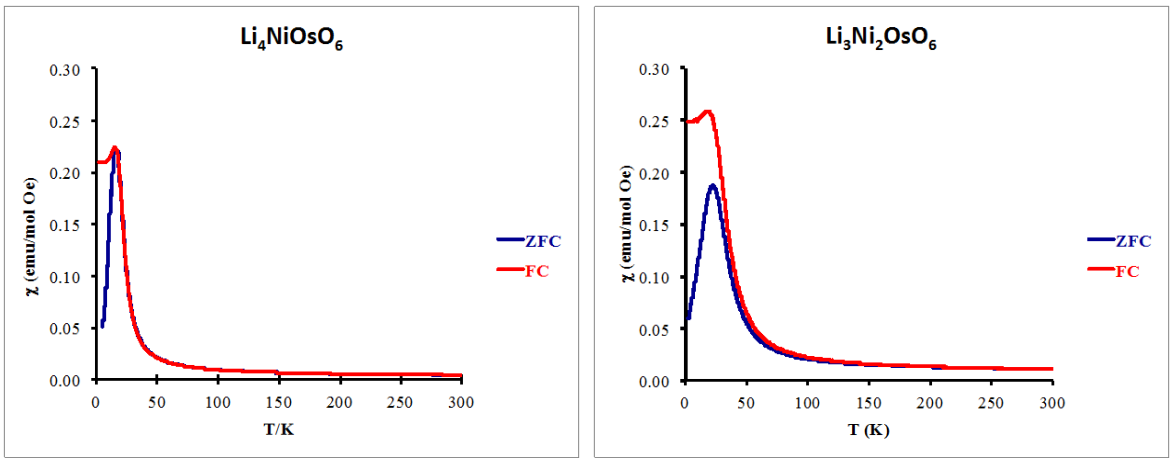

Figure 15. Temperature dependent ZFC and FC magnetic susceptibility data for Li_4NiOsO_6 (left) and $Li_3Ni_2OsO_6$ (right) compound between 2 K-300 K..

Long Range Antiferromagnetic Transition in Novel B-site Ordered Double Perovskite Ca_2ScOsO_6 [36]

A new Os-based *B*-site ordered double perovskite with the chemical composition of Ca_2ScOsO_6 was successfully synthesized. The crystal structure of the title compound was determined by employing the powder X-ray diffraction method and was found to crystallize in the monoclinic $P2_1/n$ space group with the cell constants of a = 5.4716(1) Å, b = 5.6165(1) Å, c = 7.8168 (1) Å, β = 89.889 (2)° (Figure 16).

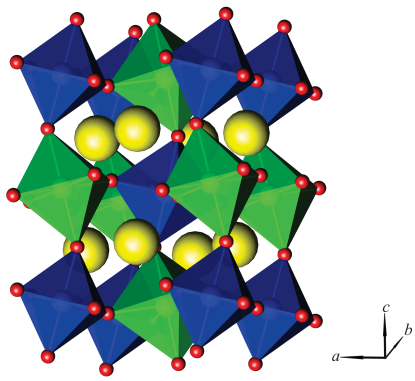

Figure 16. Polyhedral representation of the crystal structure of Ca_2ScOsO_6. The blue and green octahedra represent OsO_6^{7-} and ScO_6^{9-} units, respectively. The large yellow spheres represent Ca^{2+} ions.

The temperature dependent magnetic susceptibility data suggest that this novel $S = {}^3/_2$ compound undergoes an antiferromagnetic transition at ~69 K. Fitting the high temperature susceptibility data (100 – 300 K) to Currie-Weisse behavior showed C = 1.734 emu-K/mole (μ_{eff} = 3.72 Bohr Magnetons) and θ = -341K, which is indicative of dominant antiferromagnetic interactions (Figure 17).

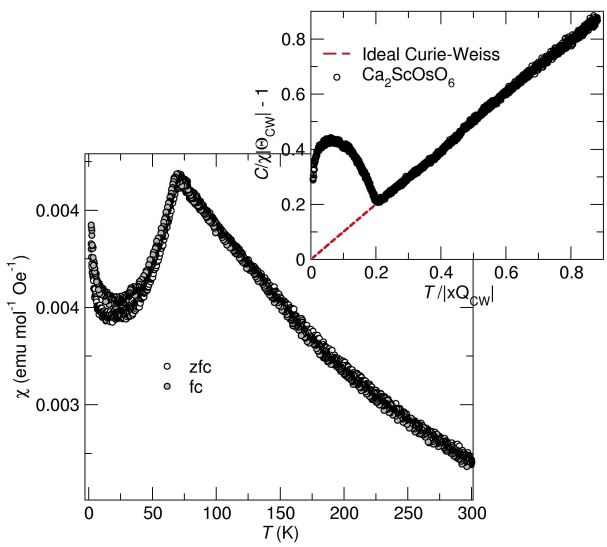

Figure 17. Temperature dependent zero-field cooled/field cooled magnetic susceptibility data for Ca_2ScOsO_6 (Lower left). Inverse magnetic susceptibility data as a function of temperature and Curie-Weiss fit in the paramagnetic region, 100K – 300K (Upper right)

Temperature-dependent specific heat measurements exhibit a lambda shape anomaly at 69 K, which is consistent with a long-range ordering of the spins. Due to a triangular arrangement of antiferromagnetically ordered magnetic ions, the system exhibits some degree of geometric magnetic frustration (GMF), but not strongly (Figure 18).

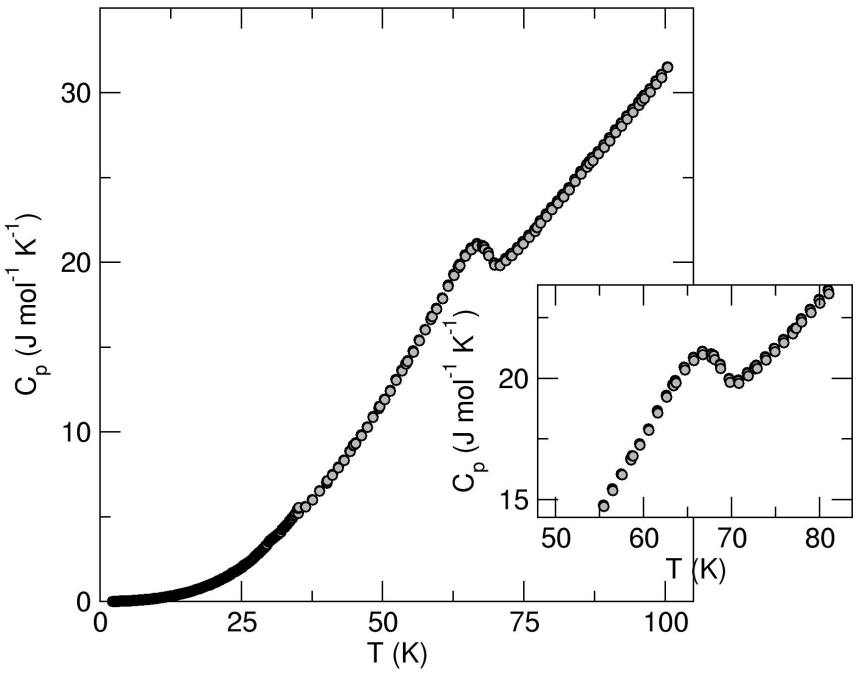

Figure 18. Temperature dependent heat capacity data for Ca_2ScOsO_6. The lambda shape anomaly is indicative of long-range order at the transition temperature.

Partial Spin Ordering and Complex Magnetic Structure in $BaYFeO_4$: A Neutron Diffraction and High Temperature Susceptibility Study [37]

Previously we studied the novel quaternary compound in the Ba-Y-Fe-O phase diagram was synthesized by solid state reaction and its crystal structure was characterized using powder X-ray diffraction. The crystal structure of $BaYFeO_4$ consists of a unique arrangement of Fe^{3+} magnetic ions, which is based on alternate corner-shared units of $[FeO_5]^{7-}$ square pyramids and $[FeO_6]^{9-}$ octahedra. This results in the formation of stairwise channels of FeO polyhedra along the *b* crystallographic axis. The structure is described in an orthorhombic crystal system in the space group *Pnma* with lattice parameters a = 13.14455(1) Å, b = 5.694960(5) Å, and c = 10.247630(9) Å (Figure 19). [38] The temperature-dependent magnetic susceptibility data reveals two antiferromagnetic (AFM) transitions at 33 K and 48 K. An upturn in the magnetic susceptibility data above these transitions is observed, which does not reach to its maximum even at 390K (Figure 20). The field-dependent magnetization data at both 2 K and 300 K show a nearly linear dependence and does not exhibit significant hysteresis. Heat capacity measurements between 2 K and 200 K reveal only a broad anomaly without any indication of long-range ordering. The latter data are not in good agreement with the magnetic susceptibility data, which makes it difficult to exactly determine the magnetic ground state for $BaYFeO_4$. This was the first physical property study in such a magnetic ion sub-structure. Attempts to induce mixed valent iron by lithium doping to the parent compound has not been successful, yet. If this process is done successfully, interesting electronic transport properties are expected.

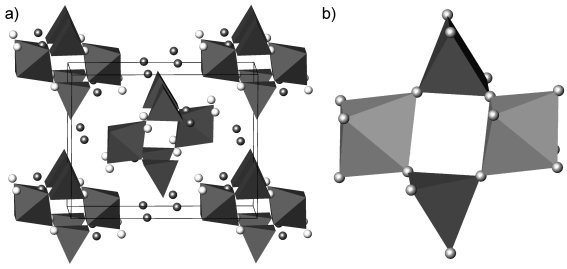

Figure 19. (a) Crystal structure of $BaYFeO_4$. View along the *b* axis. The lattice is built up from corner-shared $[FeO_5]^{7-}$ square pyramids and $[FeO_6]^{9-}$ octahedra. Barium and yttrium are shown by light grey and dark grey spheres, respectively. (b) Corner-shared octahedra and square pyramids forming $[Fe_4O_{18}]^{24-}$ rings.

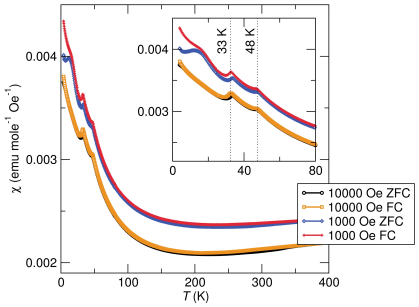

Figure 20. ZFC and FC temperature dependent magnetic susceptibility data of $BaYFeO_4$ measured under fields of 10000 and 1000 Oe. The inset shows two maxima at 33 K and 48 K. A broad maximum near 12K, observed in the 1000 Oe ZFC curve, is suppressed under high fields.

Later, variable-temperature neutron powder diffraction and high- temperature magnetic susceptibility measurements were performed to clarify the magnetic behavior. Neutron powder diffraction confirmed that the two magnetic transitions observed at 36 and 48 K are due to long-range magnetic order (Figure 21).

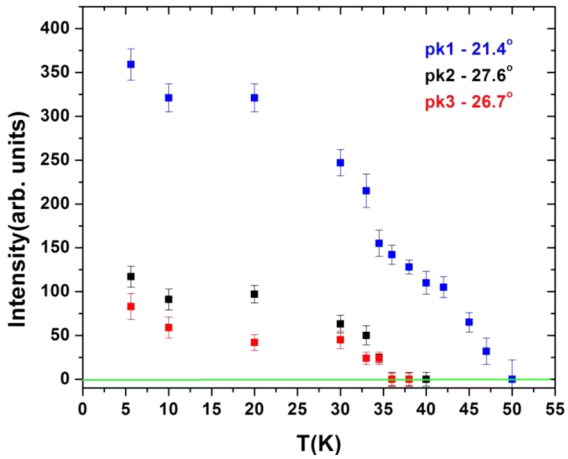

Figure 21. The relative intensities of magnetic peaks as a function of temperature. The two step intensity drops at ~ 36K and ~48K is consistent with the magnetic susceptibility data.

Below 48 K, the magnetic structure was determined as a spin-density wave (SDW) with a propagation vector, k = (0, 0, 1/3), and the moments along the b-axis (Figure 22a), whereas the structure becomes an incommensurate cycloid [k = (0, 0, ~0.35)] below 36 K with the moments within the bc-plane (Figure 22b). However, for both cases the ordered moments on Fe^{3+} are only of the order ~3.0 μ_B, smaller than the expected values near 4.5 μ_B, indicating that significant components of the Fe moments remain paramagnetic to the lowest temperature studied, 6 K. Moreover, new high-temperature magnetic susceptibility measurements revealed a peak maximum at ~550 K indicative of short-range spin correlations. It is postulated that most of the magnetic entropy is thus removed at high temperatures which could explain the absence of heat capacity anomalies at the long-range ordering temperatures. Published spin dimer

calculations, which appear to suggest a k = (0, 0, 0) magnetic structure, and allow for neither low dimensionality nor geometric frustration, are inadequate to explain the observed complex magnetic structure.

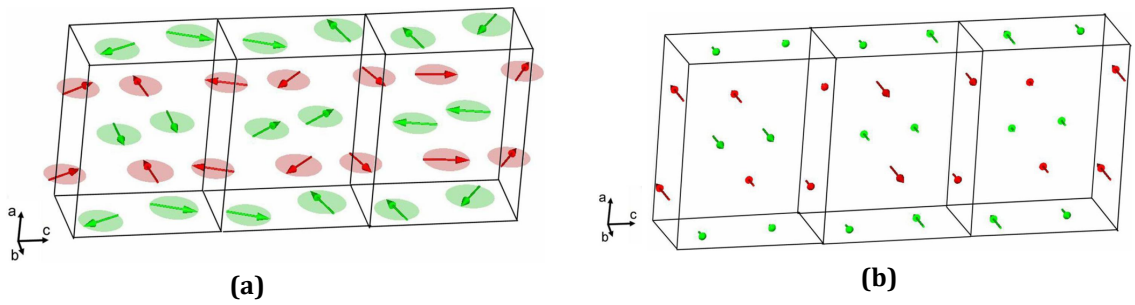

Figure 22. (a)The magnetic structures based on spin-density wave (SDW) model with a propagation vector, k = (0, 0, 1/3) below 48 K, and (b) based on an incommensurate cycloid [k = (0, 0, ~0.35)] below 36 K.

$CaYGaO_4$; a Fully Ordered Novel Olivine Type Gallate [39]

A new olivine type gallate with $CaYGaO_4$ chemical composition was synthesized. The crystal structure was determined by single crystal X-ray diffraction method. The structure is fully ordered and composed of three different motifs. CaO_6^{10-} octahedra share their edges and form one dimensional chains along the *b* crystallographic axis. The corner-shared YO_6^{9-} octahedra form puckered layers, which are extended parallel to the *bc* plane, while the GaO_4^{5-} tetrahedra are separated from each other by the octahedral units (Figure 23). The unique cation ordering in this system is related to the charge ordering between Ca^{2+} and Y^{3+} and is explained by the Pauling's rules.

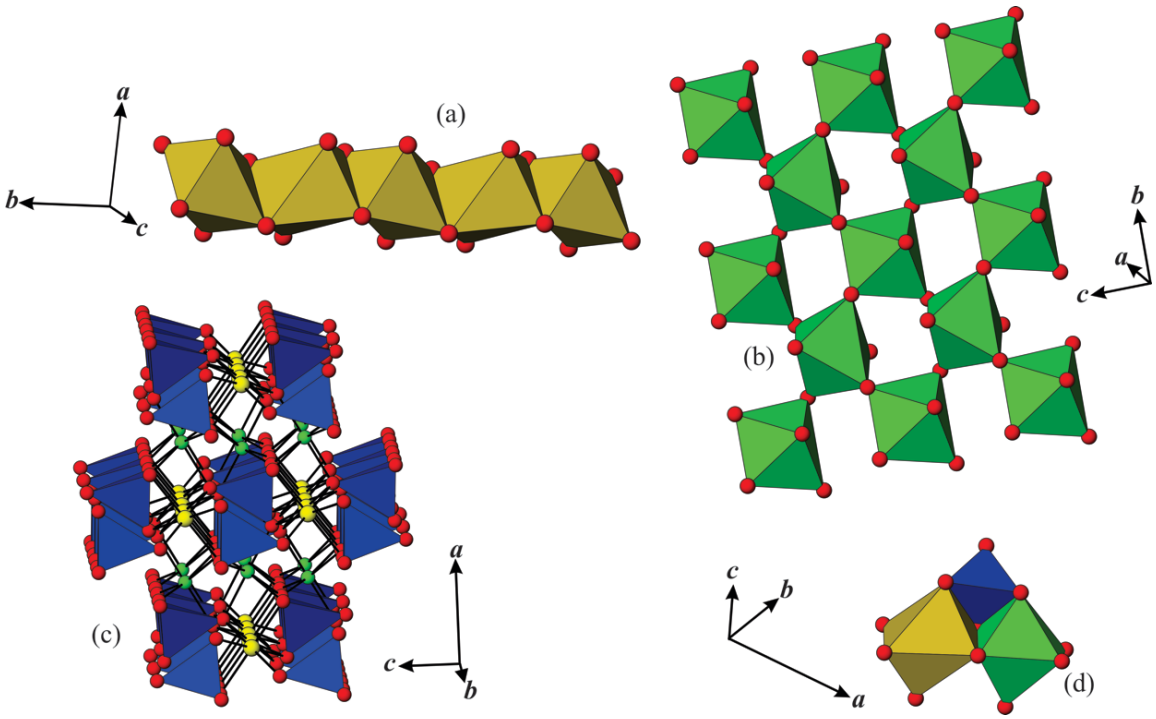

Figure 23. (a) One dimensional arrangement of edge-shared CaO_6^{10-} octahedra along the *b* crystallographic axis. (b) Corner-shared arrangement of YO_6^{9-} octahedra, forming puckered layers perpendicular to *a* crystallographic axis. (c) Discrete GaO_4^{5-} units, which are filling the empty space between the octahedra. (d) An asymmetric unit composed of three different types of polyhedra.

Partial replacement of Ga^{3+} by Fe^{3+} resulted in a series of solid solution with $CaYGa_{1-x}Fe_xO_4$ (phase range $0 < x \leq 0.50$) chemical composition. By increasing the iron content in the system *b* and *c* axes became longer while the *a* crystallographic axis

became shorter (Figure 24). The net result was a linear increase in unit cell volume in accordance with the Vegard's law (Figure 25).

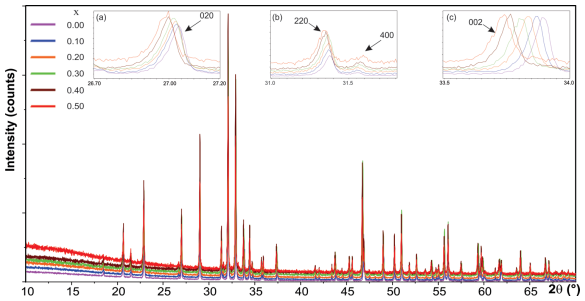

Figure 24. Experimental powder X-ray diffraction patterns for $CaYGa_{1-x}Fe_xO_4$ ($0 \leq x \leq 0.5$). The shift of 020 and 002 peaks to the lower diffraction angles and the shift of 400 peaks to the higher diffraction angles are represented in insets (a), (c) and (b), respectively.

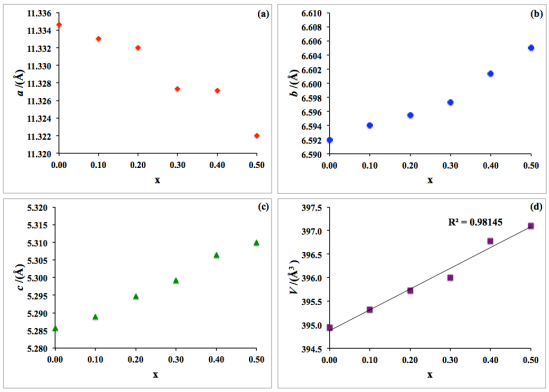

Figure 25. Cell constants and unit cell volume of $CaYGa_{1-x}Fe_xO_4$ ($0 \leq x \leq 0.5$), as a function of x. (a) Decrease of *a* axis by increasing x. (b) and (c) Show the increase in *b* and *c* axes by increasing x. (d) Linear behavior of unit cell volume by changing x in accordance with the Veggard's law.

Synthesis, Crystal Structure and Physical Properties of $La_3Al_{1-x}Si_xCuQ_7$ (Q =S, Se) [40]

Transition metal chalcogenides with the chemical composition of $La_3Al_{1-x}Si_xCuQ_7$ (Q = S, Se) were synthesized through the use of a high temperature solid-state method. Crystal structures of the title compounds were determined by X-ray single crystal and powder diffraction techniques. They were known to crystallize in a hexagonal space group $P6_3$ and are isostructural to the acentric Si-based compound, La_3SiCuQ_7 (Figure 26a). The crystal structure is composed of one-dimensional chains of trigonal planar $[CuQ_3]^{5-}$ units, which are arranged in a staggered fashion (Figure 26b).

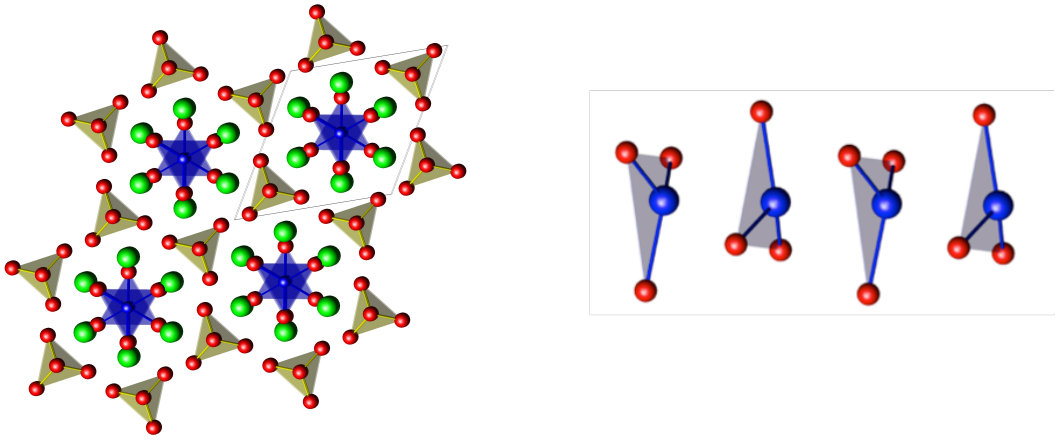

(a) **(b)**

Figure 26. (a) Hexagonal crystal structure of La_3SiCuQ_7, the unit cell is contained in the outlined box. (b) 1-D chains of equidistant staggered $[CuQ_3]^{5-}$ units.

In an attempt to induce magnetism into these diamagnetic polar systems, a partial replacement of the Si^{4+} ions with with Al^{3+} ions will result in partial oxidation of copper centers towards Cu^{2+} ($3d^9$) centers, when x = 1. When x = 0.5, The presence of unpaired electron in alternating copper centers is expected to result in interesting electronic transport properties (Peierls distortion). The effort was devoted to prepare the single-phase compounds, which will enable further physical properties measurements. The target sulfide phases that were synthesized (with side products) that were analogous to the parent compound, in that they crystallized in a hexagonal $P6_3$ crystal system. The target selenide phases were also synthesized (with side products) and it was found that

the crystal structure changed as more aluminum was introduced in to the system. The phase changed from a hexagonal $P6_3$ to a lower symmetry doubled supercel monoclinic $P2_1$ in $La_3Al_{0.75}Si_{0.25}CuSe_7$. This can be attributed to the integration of a second unique copper center, which is arranged in a different pattern. The first copper center is still retained as having a linear chain of staggered trigonal planar $[CuSe_3]^{-4.25}$ units. However, the second unique copper chain still contains the trigonal planar copper units, but are in a zig-zag formation as shown in Figure 27a. The presence of the two different coordination environment around copper centers is the driving force for doubling the unit cell, compared to the hexagonal parent structure (Figure27b). This is an interesting discovery, which may lead to exotic electronic transport transition properties. At the moment we are trying to produce phase pure samples of these compounds in order to examine their physical properties. These compounds can also be manipulated to include other transition metals and possible tellurium. But an even more interesting experiment would be to replace the rare-earth metal with the other lanthanides in order to see how the *f*-orbitals will contribute and interact with the different physical properties.

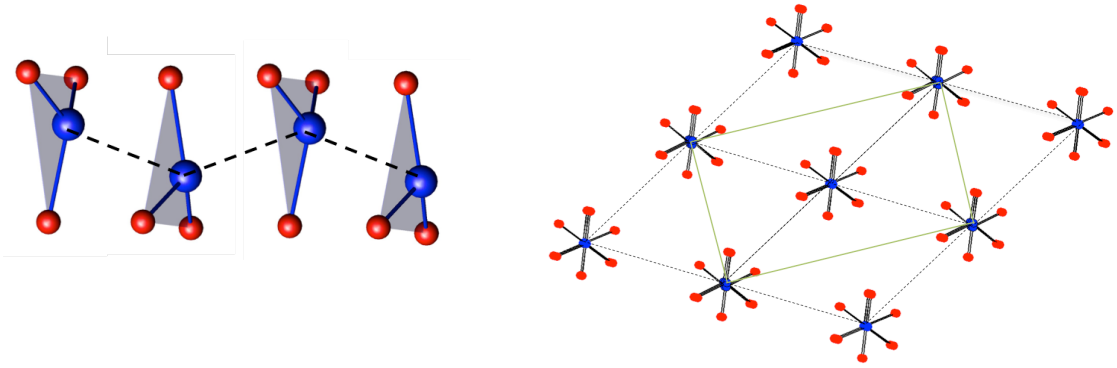

(a) **(b)**

Figure 26. (a) The distorted chain of the partially oxidized copper centers and (b) the structural transformation from hexagonal (black dashed lines) to monoclinic (nearly orthorhombic, green solid line) in Al substituted phase.

References

1. M. M. Qazilbash, *et al*. Mott transition in VO2 revealed by infrared spectroscopy and nano-imaging. *Science* **318,** 1750–3 (2007).
2. S. Mastel *et al*. Real-space mapping of nanoplasmonic hotspots via optical antenna-gap loading. *Appl. Phys. Lett*. 101, 131102 (2012)
3. Zhu et al. Temperature Gated Thermal Rectifier for Active Heat Flow Control. *Nature Materials 2013, Zhu et al (2013) submitted*.
4. S. Grefe *et al*. Near-field spatial mapping of strongly interacting multiple plasmonic infrared antennas. *MANUSCRIPT ID: CP-ART-07-2013-053104.R1 PCCP, 2013*
5. S. Grefe *et al*. Near-field Nanoscale Investigation of Optical Properties of Bi2Se3 Thin-films. 2013 MRS Spring Meeting proceedings.

6. Y. Abate, J. I. Ziegler, S. Gamage, M. H. Javani, M. I. Stockman & R. F. Haglund, *Control of Plasmonic Nanoantennas by Reversible Metal-Insulator Transition*, Scientific Reports **5,** 13997 (2015).
7. S. Lee, C. Cheng, H. Guo, K. Hippalgaonkar, K. Wang, J. Suh, K. Liu, and J. Wu, *Axially Engineered Metal-Insulator Phase Transition by Graded Doping Vo2 Nanowires*, Journal of the American Chemical Society **135**, 4850-4855 (2013).
8. Y. Abate, L. Zhen, S. B. Cronin, H. Wang, V. Babicheva, M. H. Javani, M. I. Stockman, *Nanoscopy Reveals Metallic Black Phosphorus*, arXiv:1506.05431 [cond-mat.mes-hall] (*under review* Nature Nanotechnology) (2015).
9. F. Xia, H. Wang, D. Xiao, M. Dubey, and A. Ramasubramaniam, *Two-Dimensional Material Nanophotonics*, Nat. Phot. **8**, 899-907 (2014).
10. K. S. Novoselov, A. K. Geim, S. V. Morozov, D. Jiang, M. I. Katsnelson, I. V. Grigorieva, S. V. Dubonos, and A. A. Firsov, *Two-Dimensional Gas of Massless Dirac Fermions in Graphene*, Nature **438**, 197-200 (2005).
11. K. S. Novoselov, V. I. Falko, L. Colombo, P. R. Gellert, M. G. Schwab, and K. Kim, *A Roadmap for Graphene*, Nature **490**, 192-200 (2012).
12. A. Eckmann, J. Park, H. F. Yang, D. Elias, A. S. Mayorov, G. L. Yu, R. Jalil, K. S. Novoselov, R. V. Gorbachev, M. Lazzeri, A. K. Geim, and C. Casiraghi, *Raman Fingerprint of Aligned Graphene/H-Bn Superlattices*, Nano Letters **13**, 5242-5246 (2013).
13. Q. H. Wang, K. Kalantar-Zadeh, A. Kis, J. N. Coleman, and M. S. Strano, *Electronics and Optoelectronics of Two-Dimensional Transition Metal Dichalcogenides*, Nature Nanotechnology **7**, 699-712 (2012).
14. L. Britnell, R. M. Ribeiro, A. Eckmann, R. Jalil, B. D. Belle, A. Mishchenko, Y. J. Kim, R. V. Gorbachev, T. Georgiou, S. V. Morozov, A. N. Grigorenko, A. K. Geim, C. Casiraghi, A. H. C. Neto, and K. S. Novoselov, *Strong Light-Matter Interactions in Heterostructures of Atomically Thin Films*, Science **340**, 1311-1314 (2013).
15. Z. L. Ye, T. Cao, K. O'Brien, H. Y. Zhu, X. B. Yin, Y. Wang, S. G. Louie, and X. Zhang, *Probing Excitonic Dark States in Single-Layer Tungsten Disulphide*, Nature **513**, 214-218 (2014).
16. X. Liu, T. Galfsky, Z. Sun, F. Xia, E.-c. Lin, Y.-H. Lee, S. Kéna-Cohen, and V. M. Menon, *Strong Light–Matter Coupling in Two-Dimensional Atomic Crystals*, Nat. Phot. **9**, 30-34 (2015).
17. L. Li, Y. Yu, G. J. Ye, Q. Ge, X. Ou, H. Wu, D. Feng, X. H. Chen, and Y. Zhang, *Black Phosphorus Field-Effect Transistors*, Nature Nanotechnology **9**, 372-377 (2014).
18. T. Low, R. Roldan, H. Wang, F. N. Xia, P. Avouris, L. M. Moreno, and F. Guinea, *Plasmons and Screening in Monolayer and Multilayer Black Phosphorus*, Phys. Rev. Lett. **113**, 1068021-1068025 (2014).
19. A. Favron, E. Gaufres, F. Fossard, A.-L. Phaneuf-Lheureux, N. Y. W. Tang, P. L. Levesque, A. Loiseau, R. Leonelli, S. Francoeur, and R. Martel, *Photooxidation and Quantum Confinement Effects in Exfoliated Black Phosphorus*, Nat. Mater. **14**, 826–832 (2015).
20. K.-T. Lam and J. Guo, *Plasmonics in Strained Monolayer Black Phosphorus*, J. Appl. Phys. **117**, 113105 (2015).

21. N. Youngblood, C. Chen, S. J. Koester, and M. Li, *Waveguide-Integrated Black Phosphorus Photodetector with High Responsivity and Low Dark Current*, Nat. Phot. **doi: 10.1038/nphoton.2015.23** (2015).
22. F. N. Xia, H. Wang, and Y. C. Jia, *Rediscovering Black Phosphorus as an Anisotropic Layered Material for Optoelectronics and Electronics*, Nature Communications **5**, 4458 (2014).
23. S. P. Koenig, R. A. Doganov, H. Schmidt, A. H. C. Neto, and B. Ozyilmaz, *Electric Field Effect in Ultrathin Black Phosphorus*, Appl. Phys. Lett. **104**, 1031061-4 (2014).
24. T. Low and P. Avouris, *Graphene Plasmonics for Terahertz to Mid-Infrared Applications*, ACS Nano **8**, 1086-1101 (2014).
25. Z. Zhang and J. T. Yates, *Band Bending in Semiconductors: Chemical and Physical Consequences at Surfaces and Interfaces*, Chem Rev **112**, 5520-5551 (2012).
26. Y. Abate, S. Gamage, L. Zhen, S. B. Cronin, H. Wang, V. Babicheva, M. H. Javani, and M. I. Stockman, *Nanoscopy Reveals Metallic Black Phosphorus*, arXiv:1506.05431, 1-9 (2015).
27. J. Kim, S. S. Baik, S. H. Ryu, Y. Sohn, S. Park, B.-G. Park, J. Denlinger, Y. Yi, H. J. Choi, and K. S. Kim, Science **349**, 723-726 (2015).
28. M. I. Stockman, *Nanoplasmonics: Past, Present, and Glimpse into Future*, Opt. Express **19**, 22029-22106 (2011).
29. U. Guler, A. Boltasseva, and V. M. Shalaev, *Refractory Plasmonics*, Science **344**, 263-264 (2014).
30. P-H T. Nguyen, F. Ramezanipour, J.E, Greedan, L.M.D. Cranswick, S. Derakhshan, Inorg. Chem., **51**, 11493-11499(2012).
31. S. Derakhshan, J.E, Greedan, L.M.D. Cranswick, Phys. Rev. B., **77**, 14408/1-14408/8 (2008).
32. S. Derakhshan, J.E, Greedan, T. Katsumata, L.M.D. Cranswick, Chem. Mater. 20, 5714–5720 (2008).
33. P-H. T. Nguyen, M. C. Kemei, M. S. Tan, S. Derakhshan, submitted to Journal os Solid State Chem.
34. M. Bieringer, J. E. Greedan, G. Luke, *Phys. Rev. B*, **62**, 6521 (2000).
35. P-H. T. Nguyen Master thesis, unpublished results.
36 D. Russel, A.J. Neyer, B. C. Melot, S. Derakhshan, submitted to Inorg. Chem.
37. C.M. Thompson, J.E. Greedan, V.O. Garlea, R. Flacau, M. Tan, P-H. T. Nguyen, F. Wrobel, S. Derakhshan, Inorg. Chem., **53**, 1122 (2014).
38. F. Wrobel, M. C. Kemei, S. Derakhshan, Inorg. Chem., **52**, 2671-2677 (2013).
39. R. Clark, S. J. Zhu, X. Bu, S. Derakhshan, Journal of Alloys and Compounds, **616**, 340-344 (2014).
40. C. Sturm Master thesis, unpublished results

Summary

The performed project was centered around two separate, albeit related topics. The high-resolution infrared near-field imaging experiments were performed to better understand the origin of emergence of metal insulator transitions (MIT) in known transition metal oxides and to utilize the phase transtion states of VO_2 to control and manipulate local plasmon resonaces. First, we imaged the charge dynamics in (MIT) of both amorphous VO_2 films and stress free suspended VO_2 crystals and probed the existence of mixed phases in tapered suspended crystal VO_2 beams. Then we studied the interaction of VO_2 with plasmons. Both the film VO_2 and the crystal VO_2 were explored for local unprecedented control of local plasmon light concentrations. We have demonstrated for the first time dynamic reversible switching of VO_2 metal-insulator transition and control of plasmonic nanoantennas dipolar modes.

The other component of the work was an exploratory synthesis of novel transition metal oxides and chalcogenides, which resulted in discovery of novel phases such as $BaYFeO_4$, $CaGaYO_4$, $Li_3Mg_2OsO_6$, Li_4MgOsO_6, Li_4NiOsO_6, $Li_3Ni_2OsO_6$, $La_3Si_{1-x}Al_xCuQ_7$ (Q = S, Se) and Ca_2ScOsO_6. We successfully synthesized the single-phase samples of the above-mentioned phases and investigated their crystal structures and physical properties.